Computationally generated constitutive models for particle phase rheology in gas-fluidized suspensions

Yile Gu[1],†, **Ali Ozel**[1,2], **Jari Kolehmainen**[1] **and Sankaran Sundaresan**[1]

[1]Department of Chemical and Biological Engineering, Princeton University, Princeton, NJ 08540, USA

[2]School of Engineering and Physical Sciences, Heriot-Watt University, Edinburgh EH14 4AS, UK

Developing constitutive models for particle phase rheology in gas-fluidized suspensions through rigorous statistical mechanical methods is very difficult when complex inter-particle forces are present. In the present study, we pursue a computational approach based on results obtained through Eulerian–Lagrangian simulations of the fluidized state. Simulations were performed in a periodic domain for non-cohesive and mildly cohesive (Geldart Group A) particles. Based on the simulation results, we propose modified closures for pressure, bulk viscosity, shear viscosity and the rate of dissipation of pseudo-thermal energy. For non-cohesive particles, results in the high granular temperature T regime agree well with constitutive expressions afforded by the kinetic theory of granular materials, demonstrating the validity of the methodology. The simulations reveal a low T regime, where the inter-particle collision time is determined by gravitational fall between collisions. Inter-particle cohesion has little effect in the high T regime, but changes the behaviour appreciably in the low T regime. At a given T, a cohesive particle system manifests a lower pressure at low particle volume fractions when compared to non-cohesive systems; at higher volume fractions, the cohesive assemblies attain higher coordination numbers than the non-cohesive systems, and experience greater pressures. Cohesive systems exhibit yield stress, which is weakened by particle agitation, as characterized by T. All these effects are captured through simple modifications to the kinetic theory of granular materials for non-cohesive materials.

Key words: kinetic theory, particle/fluid flow, rheology

---

1. Introduction

Eulerian models for gas–particle flows require as input a constitutive model for the particle phase stress. A great deal of work has been done in the literature on the development of constitutive models by adapting the kinetic theory of dense gases to particulate flows. The earliest and most widely used kinetic-theory models have been derived for flows of inelastic, smooth, frictionless spheres with no effects from interstitial fluid (Jenkins & Savage 1983; Lun *et al.* 1984; Jenkins & Richman 1985*b*;

† Email address for correspondence: yi.yile.gu@gmail.com

Gidaspow 1994; Garzó & Dufty 1999). They have been extended or modified to account for particle roughness (Lun 1991; Kumaran 2006; Chialvo & Sundaresan 2013; Yang, Padding & Kuipers 2016), dense regime (Chialvo & Sundaresan 2013; Berzi & Vescovi 2015), decomposition of particle fluctuations into correlated and uncorrelated parts (Février, Simonin & Squires 2005; Fox 2014), role of the interstitial fluid (Koch 1990; Gidaspow 1994; Balzer, Boëlle & Simonin 1995; Boëlle, Balzer & Simonin 1995; Ma & Kato 1998; Koch & Sangani 1999; Lun & Savage 2003; Garzó *et al.* 2012) and cohesion (Gidaspow & Huilin 1998; Kim & Arastoopour 2002; Ye, Van Der Hoef & Kuipers 2005; Van Wachem & Sasic 2008; Takada, Saitoh & Hayakawa 2016; Kellogg *et al.* 2017).

An alternative way to simulate granular flows is through the discrete element method (DEM) (Cundall & Strack 1979). Its strength lies in its flexibility to directly include the particle size distribution (Rognon *et al.* 2007; Tripathi & Khakhar 2011; Gu, Ozel & Sundaresan 2016*c*), complex particle–particle interactions including van der Waals forces (Rognon *et al.* 2008; Gu, Chialvo & Sundaresan 2014), electrostatic forces (Kolehmainen *et al.* 2016), capillary forces (Forsyth, Hutton & Rhodes 2002), liquid bridges (Boyce *et al.* 2017), solid bridges (Kuwagi, Mikami & Horio 2000) or a combination thereof (Gu, Ozel & Sundaresan 2016*b*). However, such a method becomes impractical for a large number of particles, and consequently there have been efforts to deduce continuum rheological models based on DEM simulations (Campbell 2002; MiDi 2004; da Cruz *et al.* 2005; Jop, Forterre & Pouliquen 2006; Olsson & Teitel 2007; Rognon *et al.* 2008; Otsuki & Hayakawa 2009; Sun & Sundaresan 2011; Gu *et al.* 2014, 2016*c*). Most of these simulations used to deduce models are based on particle-only DEM simulations where particles are sheared or flow down a slope. The deficiencies of these resultant models when applied to fluid–solid flows are threefold. First, the effects of the interstitial fluid are not accounted for in these DEM simulations. Second, these simulations are mostly one-dimensional in nature, and thus the effects of dilation and compaction of the particle phase are not probed adequately. Third, it has been reported in several studies (Gu *et al.* 2014; Takada, Saitoh & Hayakawa 2014; Saitoh, Takada & Hayakawa 2015) that local complex flow structures would form when cohesive forces are included in these simulations, whose effects are not fully captured by these nearly one-dimensional flows.

These deficiencies can be addressed through Eulerian–Lagrangian simulations, where the local-average equations of the fluid phase are solved using Eulerian grids and the motion of the particles is followed through DEM (an approach commonly referred to as CFD (computational fluid dynamics)-DEM in the literature). Indeed, CFD-DEM simulations have been used to deduce models for systems such as dilute gas–solid turbulent flows (Capecelatro, Desjardins & Fox 2014, 2015, 2016*a*,*b*) and granular flows in bedload transport (Maurin, Chauchat & Frey 2016).

In this paper, we seek to deduce a rheological model for granular materials in fluidized suspensions from CFD-DEM simulations. First, we consider the case of non-cohesive particles fluidized by gas (§ 3.1), and demonstrate that the approach yields models that are consistent with the analytically derived kinetic theory models, which indicates the validity of the methodology. We also show intriguing results that were previously not observed through traditional methods, such as the dependency of bulk viscosity on the state of dilation or compaction and the gravity dependence of stress. Then, we demonstrate that this methodology can be used to cases where complex inter-particle interaction is important (§ 3.2). We use the van der Waals force as an example, which is known to affect flow behaviours of Geldart Group A particles (Geldart 1973) that are frequently encountered in industry. We show that

this approach yields results that are consistent with previous studies of cohesive particles (Rognon *et al.* 2008; Gu *et al.* 2014; Irani, Chaudhuri & Heussinger 2014), thus further corroborating the methodology. Different from these studies, the present methodology is able to probe a wider parameter space. We then propose an adaptation of the kinetic-theory-based model for granular flows in the presence of van der Waals interaction between particles. This methodology can be readily applied to systems where other complex inter-particle interactions are present.

2. Mathematical modelling and flow configurations

2.1. *Mathematical modelling*

For fluidization simulations through CFD-DEM, the gas phase equations are solved using an OpenFOAM-based computational fluid dynamics solver (OpenCFD 2013), while the particle phase DEM equations are evolved via the LIGGGHTS platform (Kloss *et al.* 2012). The two phases are coupled via CFDEMcoupling (Zhou *et al.* 2010; Goniva *et al.* 2012; Kloss *et al.* 2012).

In DEM (Cundall & Strack 1979), particles are tracked by solving Newton's equations of motion:

$$m_i \frac{\mathrm{d}\boldsymbol{v}_i}{\mathrm{d}t} = \sum_j (\boldsymbol{f}_{c,ij}^n + \boldsymbol{f}_{c,ij}^t) + \sum_k \boldsymbol{f}_{v,ik} + \boldsymbol{f}_{g \to p,i} + m_i \boldsymbol{g}, \quad (2.1)$$

$$I_i \frac{\mathrm{d}\boldsymbol{\omega}_i}{\mathrm{d}t} = \sum_j \boldsymbol{T}_{t,ij}. \quad (2.2)$$

In the equations, particle i has mass m_i, moment of inertia I_i, translational and rotational velocities $\boldsymbol{v}_i$ and $\boldsymbol{\omega}_i$. There are several forces acting on the particle i. $\boldsymbol{f}_{c,ij}^n$ and $\boldsymbol{f}_{c,ij}^t$ are the normal and tangential contact forces from the collision of two particles i and j. $\boldsymbol{f}_{v,ik}$ is the van der Waals force from the interactions between two particles i and k. $\boldsymbol{f}_{g \to p,i}$ is the total interaction force on the particle i due to surrounding gas (explained further below). $m_i \boldsymbol{g}$ is the gravitational force. The torque acting on particle i due to particle j is $\boldsymbol{T}_{t,ij}$, which results from the tangential force and is equal to $\boldsymbol{R}_{ij} \times \boldsymbol{f}_{c,ij}^t$. $\boldsymbol{R}_{ij}$ is the vector from the centre of particle i to the contact point. Rolling friction is not accounted for in the present simulations.

The particle contact forces $\boldsymbol{f}_{c,ij}^n$ and $\boldsymbol{f}_{c,ij}^t$ are calculated using a Hertzian contact model as shown below (Johnson 1987; Renzo & Maio 2004):

$$\boldsymbol{f}_{c,ij}^n = \tfrac{4}{3} Y^* \sqrt{r^*} \delta_n^{3/2} \boldsymbol{n}_{ij} + 2\sqrt{\tfrac{5}{6}} \beta \sqrt{S_n m^*} \boldsymbol{v}_{ij}^n, \quad (2.3)$$

$$\boldsymbol{f}_{c,ij}^t = \begin{cases} -8G^* \sqrt{r^* \delta_n} \boldsymbol{t}_{ij} + 2\sqrt{\tfrac{5}{6}} \beta \sqrt{S_t m^*} \boldsymbol{v}_{ij}^t & \text{for } |\boldsymbol{f}_{c,ij}^t| < \mu_p |\boldsymbol{f}_{c,ij}^n| \\ -\mu_p |\boldsymbol{f}_{c,ij}^n| \dfrac{\boldsymbol{t}_{ij}}{|\boldsymbol{t}_{ij}|} & \text{for } |\boldsymbol{f}_{c,ij}^t| \geqslant \mu_p |\boldsymbol{f}_{c,ij}^n|, \end{cases} \quad (2.4)$$

where

$$\frac{1}{Y^*} = \frac{1 - \nu_i^2}{Y_i} + \frac{1 - \nu_j^2}{Y_j}, \quad \frac{1}{r^*} = \frac{1}{r_i} + \frac{1}{r_j}, \quad (2.5a,b)$$

$$\beta = \frac{\ln(e_p)}{\sqrt{\ln^2(e_p) + \pi^2}}, \quad S_n = 2Y^* \sqrt{r^* \delta_n}, \quad (2.6a,b)$$

$$\frac{1}{G^*} = \frac{2(2 + \nu_i)(1 - \nu_i)}{Y_i} + \frac{2(2 + \nu_j)(1 - \nu_j)}{Y_j}, \quad S_t = 8G^*\sqrt{r^*\delta_n}. \quad (2.7a,b)$$

The subscripts i, j denote spherical particle i or j, and the superscript $*$ denotes the effective particle property of those two particles. The effective particle mass m^* is calculated as $m^* = m_i m_j / (m_i + m_j)$; δ_n is the normal overlap distance; $\boldsymbol{n}_{ij}$ represents the unit normal vector pointing from particle j to particle i; $\boldsymbol{v}_{ij}^n$ represents the normal velocity of particle j relative to particle i; $\boldsymbol{t}_{ij}$ represents the tangential displacement obtained from the integration of the relative tangential velocity during the contact, $\boldsymbol{v}_{ij}^t$; and μ_p is the particle sliding friction coefficient. Here, Y is Young's modulus, G is the shear modulus, ν is Poisson's ratio and r is the particle radius.

The van der Waals force $\boldsymbol{f}_{v,ik}$ between particles i an k is modelled as,

$$\boldsymbol{f}_{v,ik} = -f_{v,ik}\boldsymbol{n}_{ik} = \begin{cases} -F_{vdw}(A, s)\boldsymbol{n}_{ik} & \text{for } s_{min} < s < s_{max}, \\ -F_{vdw}(A, s_{min})\boldsymbol{n}_{ik} & \text{for } s \leqslant s_{min}. \end{cases} \quad (2.8)$$

Here, F_{vdw} is the magnitude of the van der Waals force given by

$$F_{vdw}(A, s) = \frac{A}{3}\frac{2r_i r_k(r_i + r_k + s)}{s^2(2r_i + 2r_k + s)^2}\left[\frac{s(2r_i + 2r_k + s)}{(r_i + r_k + s)^2 - (r_i - r_k)^2} - 1\right]^2, \quad (2.9)$$

where A is the Hamaker constant (Hamaker 1937) which depends on the material properties (Israelachvili 2010), and s is the distance between the particle surfaces. It is assumed that the force saturates at a minimum separation distance, s_{min}, which corresponds to typical inter-molecular spacing (Yang, Zou & Yu 2000). This constant maximum force is also applied when the particles are in contact. As the magnitude of the van der Waals force decreases rapidly as the distance between the surfaces increases, a maximum cutoff distance $s_{max} = (r_i + r_k)/4$ (Aarons & Sundaresan 2006) is employed to speed up the simulation. For $s > s_{max}$, the van der Waals force is not accounted for.

To accelerate the computations, simulations typically employ a soft Young's modulus (Y^S) that is much smaller than the real value (Y^R). The superscript S denotes that the parameter corresponds to the case where a soft Young's modulus is used, and the superscript R denotes that the parameters correspond to real particle properties. However, as shown previously (Moreno-Atanasio, Xu & Ghadiri 2007; Kobayashi *et al.* 2013; Gu, Ozel & Sundaresan 2016*a*; Liu *et al.* 2016; Wilson, Dini & van Wachem 2016; Murphy & Subramaniam 2017), this cohesion model (2.8) would yield simulation results that are dependent on the Young's modulus of the particle. Thus, the cohesion model must be modified if one wishes to soften the particles without significantly affecting the simulation results. A modified cohesion model has been developed (Gu *et al.* 2016*a*) based on conserving the cohesive energy to produce results that are insensitive to Young's modulus. This modified cohesion model, shown below, is used in the simulations:

$$\boldsymbol{f}_{v,ik}^M = -f_{v,ik}^M\boldsymbol{n}_{ik} = \begin{cases} -F_{vdw}(A^R, s - s_o)\boldsymbol{n}_{ik} & \text{for } s_{min}^S < s < s_{max} \equiv (r_i + r_k)/4 \\ -F_{vdw}(A^S, s_{min}^R)\boldsymbol{n}_{ik} & \text{for } s \leqslant s_{min}^S. \end{cases} \quad (2.10)$$

Here, $A^S = A^R\theta$, where θ is $(Y^S/Y^R)^{2/5}$; s_{min}^S is the minimum separation distance for soft Young's modulus and s_o is an additional model parameter. They can be found by solving the following equations:

$$F_{vdw}(\theta, s_{min}^R) = F_{vdw}(1, s_{min}^S - s_o), \tag{2.11}$$

$$F_{vdw}(1, s_{min}^R)s_{min}^R + \int_{s_{min}^R}^{s_{max}} F_{vdw}(1, s) \, \mathrm{d}s = f_{v,ik}(\theta, s_{min}^R)s_{min}^S + \int_{s_{min}^S}^{s_{max}} F_{vdw}(1, s - s_o) \, \mathrm{d}s. \tag{2.12}$$

It should be noted that the applicability of this modified cohesion model (Gu *et al.* 2016*a*) is restricted to weakly cohesive Geldart Group A particles (Geldart 1973). Strongly cohesive Geldart Group C particles tend to form large agglomerates and are difficult to suspend via fluidization. As shown by Gu *et al.* (2016*a*), the modified cohesion model captures the bed dynamics satisfactorily in the case of Group A particles, but not the Group C particles. In the present study we focus only on Group A particles.

The fluid phase is modelled by solving the following conservation of mass and momentum equations in terms of the locally averaged variables:

$$\frac{\partial}{\partial t}(1 - \phi) + \nabla \cdot [(1 - \phi)\boldsymbol{u}_g] = 0, \tag{2.13}$$

$$\rho_g(1 - \phi)\left(\frac{\partial \boldsymbol{u}_g}{\partial t} + \boldsymbol{u}_g \cdot \nabla \boldsymbol{u}_g\right) = -\nabla p_g + \nabla \cdot \boldsymbol{\tau}_g + \boldsymbol{\Phi}_d + \rho_g(1 - \phi)\boldsymbol{g}. \tag{2.14}$$

Here, ρ_g is the density of the gas which is assumed to be constant, ϕ is the particle volume fraction, $\boldsymbol{u}_g$ is the gas velocity, p_g is the gas phase pressure, $\boldsymbol{\tau}_g$ is the gas phase deviatoric stress tensor. The total gas–particle interaction force per unit volume of the mixture $-\boldsymbol{\Phi}_d$, exerted on the particles by the gas, is composed of a generalized buoyancy force due to the slowly varying (in space) local-average gas phase stress $(-p_g\boldsymbol{I} + \boldsymbol{\tau}_g)$ and the force due to the rapidly varying flow (in space) field around the particles.

In finite-volume-method-based computations employed in our simulations, $\boldsymbol{\Phi}_d$ in any computational cell is related to $\boldsymbol{f}_{g \to p,i}$ of all the particles in that cell as $\boldsymbol{\Phi}_d = -\sum_{i \in cell} \boldsymbol{f}_{g \to p,i}/V_c$ where V_c is the volume of the computational cell. On a per particle basis, the total interaction force on the particle by the gas can be written as $\boldsymbol{f}_{g \to p,i} = -V_{p,i}\nabla p_g|_{\boldsymbol{x}=\boldsymbol{x}_{p,i}} + V_{p,i}\nabla \cdot \boldsymbol{\tau}_g|_{\boldsymbol{x}=\boldsymbol{x}_{p,i}} + \boldsymbol{f}_{d,i}$, where $V_{p,i}$ is the particle volume and $\boldsymbol{f}_{d,i}$ is the drag force calculated by the Wen & Yu (1966) drag law. As discussed in appendix B, particle phase stress extracted from the simulations is not sensitive to the drag law used in the simulations. Here, $|_{\boldsymbol{x}=\boldsymbol{x}_{p,i}}$ denotes that the Eulerian variable is interpolated to the location of particle i. The gas phase deviatoric stress tensor contribution is relatively insignificant in $\boldsymbol{f}_{g \to p,i}$ for modelling gas-fluidized beds of particles (Agrawal *et al.* 2001) and is hence ignored.

2.2. *Flow configurations*

We perform simulations in periodic domains in which one can examine the flow dynamics without wall-induced restrictions. To drive the flow in this periodic domain, we decompose the pressure term p_g in equation (2.14) into two components as follows: $p_g(\boldsymbol{x}, t) = p_g''(\boldsymbol{x}, t) - \bar{\rho}|\boldsymbol{g}|(z - z_o)$. Here, p_g'' is the computed gas pressure that obeys the periodic boundary condition and $\bar{\rho}|\boldsymbol{g}|(z - z_o)$ represents the mean vertical pressure drop due to the total mass of a two-phase mixture; $\bar{\rho}$ is the domain-averaged mixture density; z is the coordinate in the direction that is opposite of gravity and z_o is a reference elevation.

Although we will present our results in dimensionless form, it is useful to present typical dimensional quantities to demonstrate that the simulations have been done for gas–particle systems of practical interest. With this in mind, in table 1, we present the simulation parameters in both dimensional and dimensionless form. Simulations were performed for two domain-averaged particle volume fractions $\langle \phi \rangle = 0.1$ and 0.3 with different values of particle diameter and acceleration due to gravity (which was lowered to help probe relevant dimensionless groups). The simulations were run for a sufficiently long duration ($10\tau_p^{St}$) to ensure that a statistical steady state is reached (see table 1 for the definition of τ_p^{St}). Subsequently, snapshots were collected at every τ_p^{St} time instant for a duration of $20\tau_p^{St}$. Snapshots of the particle volume fraction fields obtained in simulations with different domain-averaged particle volume fractions for non-cohesive particles with $Fr_p = 65$ are shown in figure 1. The computational data from these snapshots were then post-processed to compute the particle phase stress $\boldsymbol{\sigma}$ and granular temperature T for each cell with a volume of V_c:

$$\boldsymbol{\sigma} = \frac{1}{V_c} \sum_{i \in cell} \left[\sum_{j \in cell, (j \neq i)} \frac{1}{2} \boldsymbol{r}_{ij} \otimes \boldsymbol{f}_{ij} + m_i (\boldsymbol{v}_i - \boldsymbol{u}_s|_{\boldsymbol{x}=\boldsymbol{x}_i}) \otimes (\boldsymbol{v}_i - \boldsymbol{u}_s|_{\boldsymbol{x}=\boldsymbol{x}_i}) \right], \qquad (2.15)$$

and

$$T = \frac{1}{3} \sum_{i \in cell} [(\boldsymbol{v}_i - \boldsymbol{u}_s|_{\boldsymbol{x}=\boldsymbol{x}_i}) \cdot (\boldsymbol{v}_i - \boldsymbol{u}_s|_{\boldsymbol{x}=\boldsymbol{x}_i})], \qquad (2.16)$$

where $\boldsymbol{r}_{ij}$ is the centre-to-centre contact vector from particle j to particle i, $\boldsymbol{f}_{ij}$ is the total force between the two particles, $\boldsymbol{v}_i$ is the velocity of particle i and $\boldsymbol{u}_s|_{\boldsymbol{x}=\boldsymbol{x}_i}$ is the local-average particle velocity at the location of the particle, obtained by interpolating from the Eulerian velocity of the solid phase at the cell centres (more details in Ozel *et al.* (2017)). In appendix C, we present how we choose the mapping mesh size to compute the particle phase stress. In appendix D, we present how frequently local variables of granular temperature and particle volume fractions take different values; all the analyses that follow are based on a parameter space where enough statistics have been collected.

3. Simulation results

In fluidization, the normal stress in the vertical direction is usually larger than those in the lateral directions (Koch & Sangani 1999). Normal stress differences were probed briefly in this study (see appendix A) and it was found to be dependent on domain-averaged particle volume fraction $\langle \phi \rangle$ and local particle volume fraction ϕ. As the normal stress difference has not been demonstrated to be responsible for any known flow phenomena in fluidized beds, we have not probed it further in this study.

By following Goldstein, Handler & Sirovich (1993), Garzó & Dufty (1999), Jenkins & Richman (1985*a*) and Jenkins & Richman (1985*b*), the particle phase stress tensor is expressed as:

$$\boldsymbol{\sigma} = [p - \mu_b (\nabla \cdot \boldsymbol{u}_s)] \boldsymbol{I} - 2\mu_s \boldsymbol{S}, \qquad (3.1)$$

where p is pressure, μ_b is bulk viscosity, μ_s is shear viscosity and $\boldsymbol{S}$ is the rate of deformation tensor:

$$\boldsymbol{S} = \frac{1}{2} [\nabla \boldsymbol{u}_s + (\nabla \boldsymbol{u}_s)^{\mathrm{T}}] - \frac{1}{3} (\nabla \cdot \boldsymbol{u}_s) \boldsymbol{I}. \qquad (3.2)$$

Simulation parameters	Value
Domain size; $(d \times d \times d)$	$240 \times 240 \times 960$
Grid size; $(d \times d \times d)$	$3 \times 3 \times 3$
Acceleration due to gravity; g (m s^{-2})	9.81/2.45
Particle diameter; d (µm)	75/150/300
Particle density; ρ_p (kg m^{-3})	1500
Real Young's modulus; Y^R (Pa)	7×10^{10}
Soft Young's modulus used in simulations; Y^S (Pa)	10^6
Poisson's ratio; ν	0.42
Restitution coefficient; e_p	0.9
Sliding friction coefficient; μ_p	0.5
Real Hamaker constant; A^R (J)	$10^{-19}/10^{-18}$
Minimum separation distance for real Young's modulus; s_{min}^R (m)	10^{-9}
Minimum separation distance for soft Young's modulus; s_{min}^S (m)	1.641×10^{-7}
Modified cohesion model parameter; s_o (m)	1.548×10^{-7}
Gas density; ρ_g (kg m^{-3})	1.3
Gas viscosity; μ_g (Pa s)	1.8×10^{-5}
Characteristic quantities	Value
Stokes relaxation time; $\tau_p^{St} = \dfrac{\rho_p d^2}{18 \mu_g}$ (s)	0.026 ($d = 75$ µm)
	0.104 ($d = 150$ µm)
	0.417 ($d = 300$ µm)
Terminal velocity based on Wen & Yu (1966) drag law; v_t (m s^{-1})	0.219 ($d = 75$ µm; $g = 9.81$ m s^{-2})
	0.649 ($d = 150$ µm; $g = 9.81$ m s^{-2})
	1.533 ($d = 300$ µm; $g = 9.81$ m s^{-2})
	0.0597 ($d = 75$ µm; $g = 2.45$ m s^{-2})
Froude number; $Fr_p = v_t^2/(gd)$	65 ($d = 75$ µm; $g = 9.81$ m s^{-2})
	286 ($d = 150$ µm; $g = 9.81$ m s^{-2})
	799 ($d = 300$ µm; $g = 9.81$ m s^{-2})
	19 ($d = 75$ µm; $g = 2.45$ m s^{-2})
Particle Reynolds number; $Re_p = \dfrac{\rho_g v_t d}{\mu_g}$	1.18 ($d = 75$ µm; $g = 9.81$ m s^{-2})
	7.03 ($d = 150$ µm; $g = 9.81$ m s^{-2})
	33.23 ($d = 300$ µm; $g = 9.81$ m s^{-2})
	0.32 ($d = 75$ µm; $g = 2.45$ m s^{-2})
Particle Stokes number; $St_p = \dfrac{1}{18} \dfrac{\rho_p}{\rho_g} Re_p$	76 ($d = 75$ µm; $g = 9.81$ m s^{-2})
	451 ($d = 150$ µm; $g = 9.81$ m s^{-2})
	2130 ($d = 300$ µm; $g = 9.81$ m s^{-2})
	20 ($d = 75$ µm; $g = 2.45$ m s^{-2})
Bond number; $Bo^* = F_{coh}^{max}/(m_p g)$ where $F_{coh}^{max} = \dfrac{A^R d_p}{24 s_{min}^R{}^2}$	96 ($d = 75$ µm; $A^R = 10^{-19}$ J)
	960 ($d = 75$ µm; $A^R = 10^{-18}$ J)
	3840 ($d = 75$ µm; $A^R = 4 \times 10^{-18}$ J)

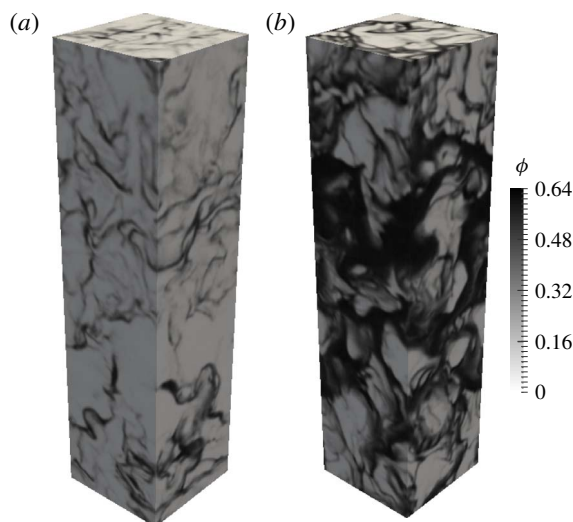TABLE 1. Computational domain and simulation parameters.

FIGURE 1. Snapshots of the particle volume fraction field in a periodic domain. Domain-averaged particle volume fraction $\langle\phi\rangle$ is (*a*) 0.1 and (*b*) 0.3. Simulation parameters are listed in table 1. Fluidization simulations of non-cohesive particles are performed with $Fr_p = 65$. Figures are taken from Ozel *et al.* (2016).

It is worth noting that only linear terms in the spatial gradients are retained in (3.1). A more rigorous way to model inhomogeneous gas–solid flows is to perform systematic derivations of the kinetic equations up to high-order terms (Burnett and super-Burnett orders) starting from the Boltzmann equation (e.g. see Sela, Goldhirsch & Noskowicz (1996), Sela & Goldhirsch (1998), Kumaran (2004, 2006)). The number of spatial derivatives in the high-order terms for the stress tensor is much more than that for Navier–Stokes level of modelling used here. They are functions of all hydrodynamic variables. Initial assessment has been performed on the isotropic part of the stress tensor (based on constitutive relations suggested by one referee), and suggests that the contributions of second-order terms are minimal. For further investigations, one would have to perform even more complex binning of the data and also include an anisotropic streaming stress tensor. These are beyond the scope of this manuscript, which seeks to deduce a simple model for cohesive systems that captures most of the effects. Thus, we choose not to directly model these higher-order terms.

Based on simulation results, we propose closures for pressure p, bulk viscosity μ_b and shear viscosity μ_s for both non-cohesive and cohesive particles. In the following, we first illustrate that the present methodology can yield results for non-cohesive particles that are consistent with analytically derived kinetic-theory models, and demonstrate the suitability of the methodology (§ 3.1). Then, we modify these closures to include cohesion (§ 3.2).

3.1. *Non-cohesive particles*

As shown in table 1, fluidization simulations with non-cohesive particles are performed for several Froude numbers corresponding to different values of particle diameter and acceleration due to gravity as well as for different domain-averaged particle volume fractions. In the model development, independent variables and scalings are carefully
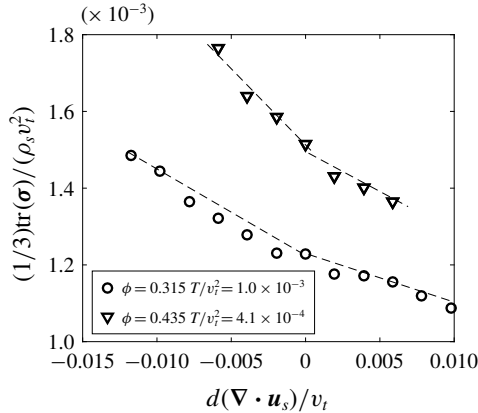
FIGURE 2. Dimensionless trace of the stress tensor versus dimensionless rate of dilation for two combinations of local particle volume fraction ($\phi = 0.315$ and 0.435) and granular temperature. In both cases, $\text{tr}(\boldsymbol{\sigma})$ exhibits a linear relationship with $\nabla \cdot \boldsymbol{u}_s$ for both $\boldsymbol{u}_s < 0$ and $\boldsymbol{u}_s > 0$ segments, as indicated by the dashed lines. Data from fluidization simulations of non-cohesive particles; $Fr_p = 799$; $\langle \phi \rangle = 0.1$.

chosen so that the stress results from these different simulations collapse, ensuring the generality of the proposed model.

3.1.1. *Pressure*

From (3.1), we have

$$\tfrac{1}{3}\text{tr}(\boldsymbol{\sigma}) = p - \mu_b \nabla \cdot \boldsymbol{u}_s. \tag{3.3}$$

As detailed in §2.2, $\boldsymbol{\sigma}$ is computed for each computational cell, and $\text{tr}(\boldsymbol{\sigma})$ is binned with particle volume fraction ϕ, granular temperature T, and rate of dilation $\nabla \cdot \boldsymbol{u}_s$.

Figure 2 shows the dimensionless trace of the stress tensor $(1/3)\text{tr}(\boldsymbol{\sigma})/(\rho_s v_t^2)$ versus the dimensionless rate of dilation $d(\nabla \cdot \boldsymbol{u}_s)/v_t$ for two combinations of particle volume fraction ϕ and dimensionless granular temperature T/v_t^2. It is found that $\text{tr}(\boldsymbol{\sigma})$ exhibits a linear relationship with $\nabla \cdot \boldsymbol{u}_s$ for both $\nabla \cdot \boldsymbol{u}_s < 0$ and $\nabla \cdot \boldsymbol{u}_s > 0$ segments. This finding is consistent with (3.3), and thus supports the suitability of the constitutive equation (3.1). Furthermore, since $\text{tr}(\boldsymbol{\sigma})$ varies substantially with $\nabla \cdot \boldsymbol{u}_s$ in the system, the pressure p is extracted from bins where $\nabla \cdot \boldsymbol{u}_s \approx 0$. It is worth noting that the flow domain is fully periodic and there is no macroscopic dilation or compression, $\langle \nabla \cdot \boldsymbol{u}_s \rangle = 0$.

Figure 3(a) shows the variation of $p/(\rho_s v_t^2)$ with T/v_t^2. It is found that p scales with T, which is consistent with the standard kinetic theory (Lun *et al.* 1984),

$$p = \rho_s H(\phi) T, \tag{3.4}$$

$$H(\phi) = \phi[1 + 4\eta\phi g_0], \tag{3.5}$$

where $\eta = (1 + e_p)/2$ and g_0 is the radial distribution function at contact.

Figure 3(b) shows a plot of $p/(\rho_s T)$ against ϕ for various Fr_p and $\langle \phi \rangle$. The data collapse onto a single curve, and it is found that the standard kinetic theory captures
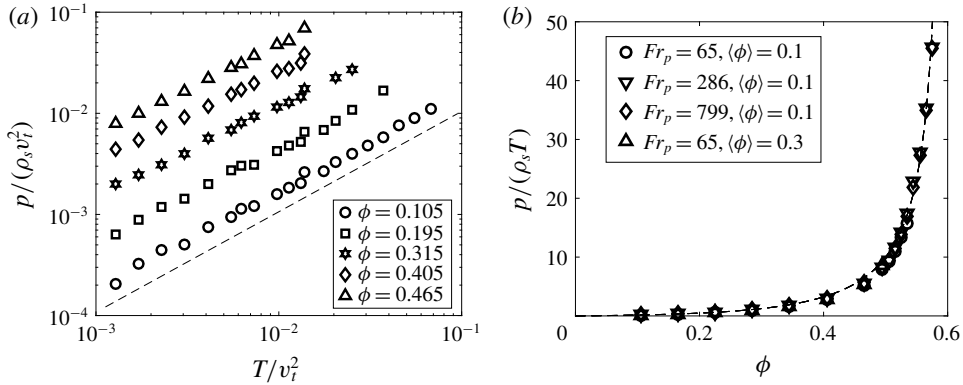
FIGURE 3. (*a*) Dimensionless pressure versus dimensionless granular temperature for various local particle volume fractions ($\phi = 0.105, 0.195, 0.315, 0.405, 0.465$). In all cases, p scales with T as indicated by the dashed line with slope of 1. Data from fluidization simulations of non-cohesive particles; $Fr_p = 65$; $\langle\phi\rangle = 0.1$. (*b*) Pressure scaled by granular temperature versus local particle volume fraction for various Froude numbers and domain-averaged particle volume fractions. Dashed line: equation (3.5).

the collapse well. Throughout this paper, we have used g_0 proposed by Chialvo & Sundaresan (2013):

$$g_0 = \frac{1 - \phi/2}{(1 - \phi)^3} + \frac{\alpha_{g_0}\phi^2}{(\phi_c - \phi)^{3/2}}, \tag{3.6}$$

where $\alpha_{g_0} = 0.58$, and ϕ_c is a jamming volume fraction that varies with the sliding friction coefficient μ_p (Chialvo, Sun & Sundaresan 2012; Chialvo & Sundaresan 2013). The jamming condition was found by Sun & Sundaresan (2011) to depend on the nature of the deformation. Simple shear appears to afford the smallest value of ϕ_c among all types of deformations. For $\mu_s = 0.5$, simple shear simulations yielded $\phi_c = 0.587$ (Chialvo *et al.* 2012). In the present simulations, where appreciable compaction and dilation are also at play, $\phi_c = 0.61$ was found to fit the data better and is used in all subsequent figures.

3.1.2. *Bulk viscosity*

According to (3.3) as well as figure 2, bulk viscosity μ_b can be found by computing the slope of $(1/3)\text{tr}(\boldsymbol{\sigma})$ versus $-\boldsymbol{\nabla} \cdot \boldsymbol{u}_s$. As indicated in the figure, the slope differs between $\boldsymbol{\nabla} \cdot \boldsymbol{u}_s < 0$ and $\boldsymbol{\nabla} \cdot \boldsymbol{u}_s > 0$. Thus, μ_b is calculated for $\boldsymbol{\nabla} \cdot \boldsymbol{u}_s < 0$ (corresponding to compaction) and $\boldsymbol{\nabla} \cdot \boldsymbol{u}_s > 0$ (corresponding to dilation) separately.

Figure 5(*a*) shows the dimensionless bulk viscosity $\mu_b/(\rho_s d v_t)$ versus T/v_t^2 for two particle volume fractions. It is found that μ_b scales with $\sqrt{T}$, which is consistent with the standard kinetic theory. According to Lun *et al.* (1984)

$$\mu_b = \left(\eta\frac{8}{3\sqrt{\pi}}\phi^2 g_0\right)\rho_s d\sqrt{T}. \tag{3.7}$$

However, unlike the standard kinetic theory, it is found that bulk viscosity is larger for compaction than for dilation for a given particle volume fraction and granular
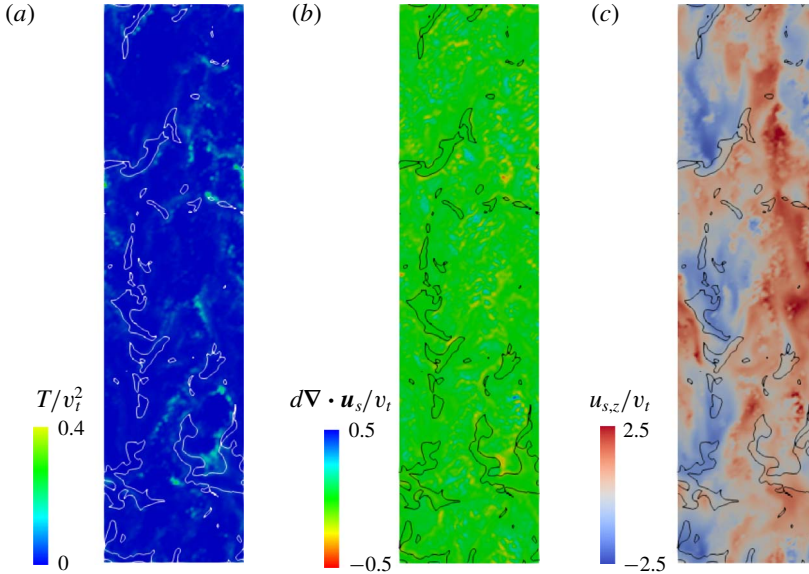
FIGURE 4. (Colour online) Snapshots of (*a*) granular temperature, (*b*) dilation/compression $\nabla \cdot \boldsymbol{u}_s$, (*c*) vertical solid velocity with local solid volume fraction iso-contours ($\phi = 0.3$). $Fr_p = 75$. Domain-averaged volume fraction $\langle \phi \rangle = 0.1$.

temperature. This behaviour of bulk viscosity has also been observed in simulations of travelling waves in particle–fluid suspensions (Moon, Kevrekidis & Sundaresan 2006; Derksen & Sundaresan 2007). One can interpret this behaviour as μ_b being a function of $\nabla \cdot \boldsymbol{u}_s / (\sqrt{T}/d)$, which is indicative of a higher-order effect.

We plot the bulk viscosity scaled by granular temperature, $\mu_b/(\rho_s d \sqrt{T})$, against ϕ for different Froude numbers Fr_p and $\langle \phi \rangle$ in figure 5(*b*). Values of bulk viscosity for compaction and those for dilation each collapse. The bulk viscosity data could be captured by

$$\mu_b = \left(\alpha_{\mu_b} \eta \frac{8}{3\sqrt{\pi}} \phi^2 g_0 \right) \rho_s d \sqrt{T}, \tag{3.8}$$

where $\alpha_{\mu_b} = 1$ for dilation and $\alpha_{\mu_b} = 1.5$ for compaction.

By following Capecelatro *et al.* (2014), snapshots of granular temperature, dilation/compression $\nabla \cdot \boldsymbol{u}_s$ and vertical solid velocity with a solid volume fraction contour ($\phi = 0.3$) were generated (see figure 4). As seen from the figure, the granular temperature is very low within falling clusters and it reaches maximum values just out of a cluster, where maximum dilation $\nabla \cdot \boldsymbol{u}_s < 0$ occurs. As discussed by Fox (2014), viscous heating due to dilation/compaction behaves as a source term for the granular temperature.

3.1.3. *Shear viscosity*

The shear viscosity, μ_s, is calculated as:

$$\mu_s = \frac{\boldsymbol{\tau} : (2\boldsymbol{S})}{(2\boldsymbol{S}) : (2\boldsymbol{S})}, \tag{3.9}$$

where the deviatoric stress tensor $\boldsymbol{\tau} = -\boldsymbol{\sigma} + (1/3)\mathrm{tr}(\boldsymbol{\sigma})\boldsymbol{I}$.
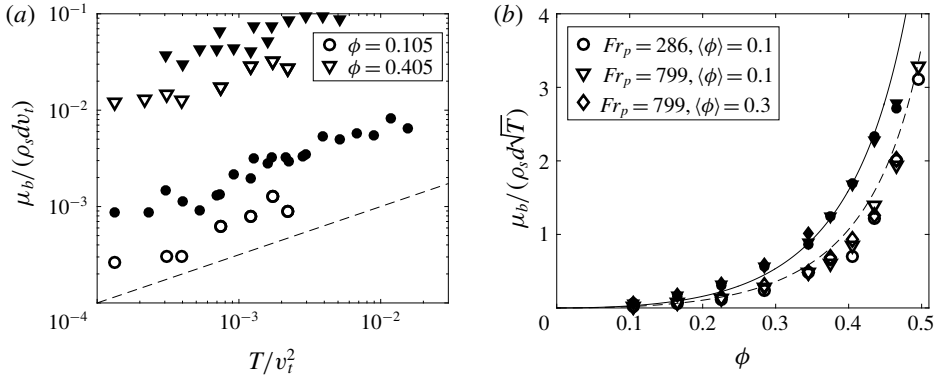
FIGURE 5. (*a*) Dimensionless bulk viscosity versus dimensionless granular temperature for two local particle volume fractions ($\phi = 0.315$ and 0.435). Filled (unfilled) symbols are for compaction (dilation). In all cases, μ_b scales with $\sqrt{T}$ as indicated by the dashed line with slope of $1/2$. Data from fluidization simulations of non-cohesive particles; $Fr_p = 799$; $\langle \phi \rangle = 0.1$. (*b*) Bulk viscosity scaled by granular temperature versus local particle volume fraction for different Froude numbers and domain-averaged particle volume fractions. Solid line: equation (3.8) with $\alpha_{\mu_b} = 1.5$. Dashed line: same equation with $\alpha_{\mu_b} = 1$.

Kinetic-theory-based models derived for gas–solid systems (Koch 1990; Gidaspow 1994; Balzer *et al.* 1995; Boëlle *et al.* 1995; Ma & Kato 1998; Koch & Sangani 1999; Lun & Savage 2003; Garzó *et al.* 2012) have taken into consideration the potential influence of the slip velocity $u_{slip} = |\boldsymbol{u}_g - \boldsymbol{u}_s|$ on shear viscosity. Therefore, in our analysis, μ_s was computed in each Eulerian grid, and initially binned with u_{slip}, ϕ and T. Figure 6 shows the dimensionless shear viscosity $\mu_s/(\rho_s d v_t)$ versus T/v_t^2 for various dimensionless slip velocities u_{slip}/v_t. Two regimes are readily identified, as indicated by the dashed lines, where μ_s scales with T in the low T regime and with $T^{1/2}$ in the high T regime. These two flow regimes are also observed in the kinetic-theory-based models derived for gas–solid systems (Koch 1990; Gidaspow 1994; Balzer *et al.* 1995; Boëlle *et al.* 1995; Ma & Kato 1998; Koch & Sangani 1999; Lun & Savage 2003; Garzó *et al.* 2012). However, unlike these studies, it is found that u_{slip} affects μ_s minimally. Therefore, μ_s was simply binned with ϕ and T.

We plot the scaled shear viscosity in the high T regime $\mu_{s,c}/(\rho_s d\sqrt{T})$ against ϕ for various Fr_p and $\langle \phi \rangle$ in figure 7(*a*). The data are consistent with the predictions of standard kinetic theory that does not account for effects of interstitial fluid (Lun *et al.* 1984):

$$\mu_{s,c} = \left(\frac{2 + \alpha_0}{6} \right) \left[\frac{5\sqrt{\pi}}{48 g_0 \eta (2 - \eta)} \left(1 + \frac{8}{5} \phi \eta g_0 \right) \left(1 + \frac{8}{5} \eta (3\eta - 2) \phi g_0 \right) \right. \\ \left. + \frac{16}{5} \eta \frac{\phi^2 g_0}{\sqrt{\pi}} \right] \rho_s d\sqrt{T}, \tag{3.10}$$

where $\alpha_0 = 1.6$. The modified kinetic theory proposed by Chialvo & Sundaresan (2013) that is based on an inertial number model in the dense regime (MiDi 2004; da Cruz *et al.* 2005; Jop *et al.* 2006) yields essentially indistinguishable predictions as (3.10), as illustrated in figure 7(*a*). This consistency again affirms the validity of the computational approach followed in the present study.
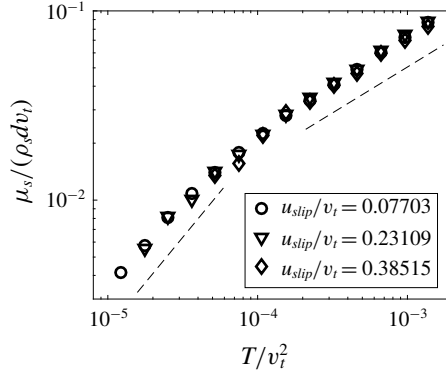
FIGURE 6. Dimensionless shear viscosity versus dimensionless granular temperature for various dimensionless slip velocities and $\phi = 0.465$. Two regimes are identified. μ_s scales with T in the low T regime and with $T^{1/2}$ in the high T regime, as indicated by the two dashed lines with slopes of 1 (left) and 1/2 (right). Data from fluidization simulations of non-cohesive particles; $Fr_p = 286$; $\langle \phi \rangle = 0.3$.
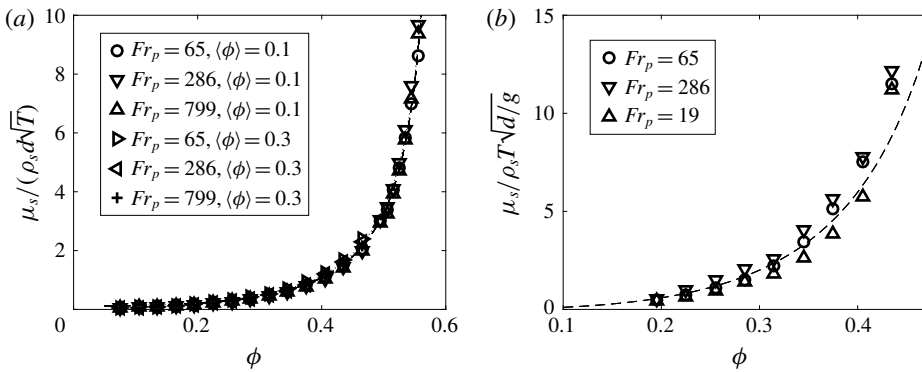

FIGURE 7. Scaled shear viscosity versus local particle volume fraction for different Froude numbers and domain-averaged particle volume fractions. (*a*) Data in the high T regime where μ_s scales with $T^{1/2}$ are plotted. Dashed line: equation (3.10). Dotted line: the modified kinetic theory proposed by Chialvo & Sundaresan (2013). (*b*) Data in the low T regime where μ_s scales with T are plotted. Dashed line: equation (3.12).

We found that shear viscosity data in the low T regime could be captured as,

$$\mu_{s,g} = f_{\mu_{s,g}}(\phi) \rho_s T \sqrt{d/g}. \tag{3.11}$$

Such a dependence of transport coefficient on gravity has also been observed before; from numerical simulations, it was found that gravity affects heat conductivity of molecular gas (Doi, Santos & Tij 1999). Figure 7(*b*) shows a plot of $\mu_s/\rho_s T \sqrt{d/g}$ against ϕ extracted from simulations performed using different particle diameters and acceleration due to gravity (which are combined in terms of Froude number). Data collapse reasonably well onto a single curve, supporting the scaling. The dashed line in figure 7(*b*) corresponds to

$$f_{\mu_{s,g}} = \alpha_{\mu_{s,g}} g_0 \phi^2, \tag{3.12}$$

where $\alpha_{\mu_{s,g}} = 8.0$.

The transition from the high T regime to the low T regime can be understood as a change in time between inter-particle collisions. $\mu_s \sim \rho_s T \tau$, where τ is a collision time for the system. At high T conditions, the collision time scales as $d/\sqrt{T}$. In the low T regime, collisions appear to be largely determined by gravitational fall and hence the $\sqrt{d/g}$ scaling for collision time. In our computationally generated model approach, we simply bridge the low and high T regimes via

$$\mu_s = \min(\mu_{s,g}, \mu_{s,c}). \tag{3.13}$$

3.1.4. *Pseudo-thermal energy balance*

As proposed kinetic-theory-based models for pressure, bulk viscosity, and shear viscosity directly depend on granular temperature, a balance of pseudo-thermal energy (PTE) of particle velocity fluctuations needs to be solved to obtain the granular temperature. In fluidized gas–particle mixtures, the rate of production of PTE by shear $-\boldsymbol{\sigma} : \nabla \boldsymbol{u}_s$ is, to a good approximation, balanced locally by the rate of dissipation of PTE by inter-particle collisions J_{coll}. Therefore, we set

$$-\boldsymbol{\sigma} : \nabla \boldsymbol{u}_s = J_{coll}. \tag{3.14}$$

This approximation is supported by the following two observations.

First, our computational results show that u_{slip} affects $-\boldsymbol{\sigma} : \nabla \boldsymbol{u}_s$ minimally, and thus all the terms that depend on u_{slip} affect the rates of generation and dissipation of PTE only in a secondary fashion; this is consistent with the high particle Stokes number, as shown in table 1. Hence any terms involving u_{slip} cannot be probed using our results. The weak role of u_{slip} is illustrated in figure 8, where the scaled rate of production of PTE by shear $-\boldsymbol{\sigma} : \nabla \boldsymbol{u}_s d/\rho_s v_t^3$ is plotted against T/v_t^2 for various u_{slip}/v_t.

Second, at high T regime, the expression for J_{coll} from the kinetic theory of granular materials is found to match $-\boldsymbol{\sigma} : \nabla \boldsymbol{u}_s$ from the simulations. This is illustrated in figure 9(*a*) where the scaled rate of production of PTE by shear $-\boldsymbol{\sigma} : \nabla \boldsymbol{u}_s d/\rho_s T^{3/2}$ is plotted against ϕ for various Fr_p and $\langle \phi \rangle$. Data collapse onto a single curve, which is described well by (3.14) where J_{coll} is equal to $J_{coll,MKT}$ from modified kinetic theory (Chialvo & Sundaresan 2013):

$$J_{coll,MKT} = \frac{12}{\sqrt{\pi}} \phi^2 g_0 (1 - e_{eff}^2) \frac{\rho_s T^{3/2}}{d}. \tag{3.15}$$

In this equation, the restitution coefficient e_p in the standard kinetic theory (Lun *et al.* 1984) is replaced by an effective restitution coefficient e_{eff} (Chialvo & Sundaresan 2013) to account for the total energy loss due to inelasticity and friction during an inter-particle collision, which is supported by analytical derivations of kinetic theory for slightly frictional particles (Jenkins & Zhang 2002). Based on simple shear simulations of frictional particles, Chialvo & Sundaresan (2013) related e_{eff} to the particle sliding friction coefficient μ_p as the following,

$$e_{eff} = e_p - \tfrac{3}{2} \mu \exp(-3\mu). \tag{3.16}$$

Both observations above suggest that the approximation $-\boldsymbol{\sigma} : \nabla \boldsymbol{u}_s = J_{coll}$ is reasonable, and therefore we formulate models for J_{coll} based on $-\boldsymbol{\sigma} : \nabla \boldsymbol{u}_s$ data from simulations, when (3.15) is not valid (e.g. as in the low T regime).
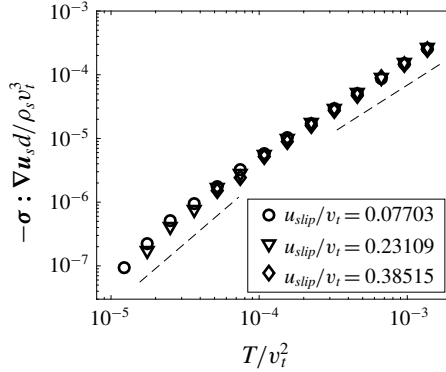
FIGURE 8. Dimensionless production rate of PTE by shear versus dimensionless granular temperature for various dimensionless slip velocities and $\phi = 0.465$. Two regimes are identified. $-\boldsymbol{\sigma} : \nabla \boldsymbol{u}_s$ scales with T^2 in the low T regime and with $T^{3/2}$ in the high T regime, as indicated by the two dashed lines with slope of 2 (left) and 3/2 (right). Data from fluidization simulations of non-cohesive particles; $Fr_p = 286$; $\langle \phi \rangle = 0.3$.
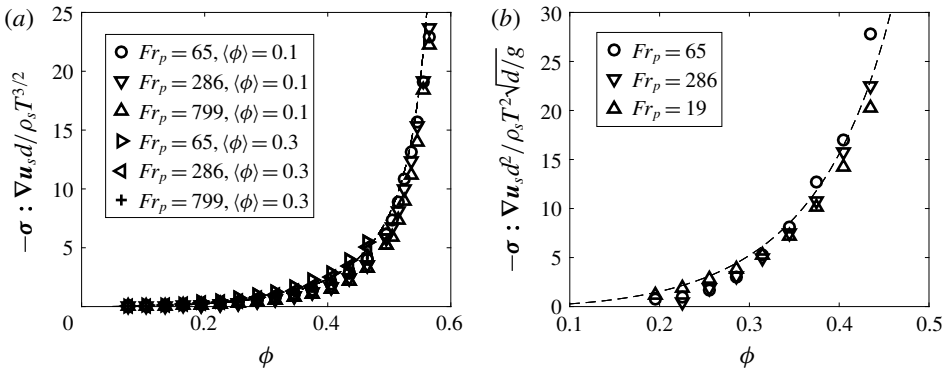

FIGURE 9. Rescaled rate of production of PTE by shear scaled versus local particle volume fraction for different Froude numbers and domain-averaged particle volume fractions. (*a*) Data in the high T regime where $-\boldsymbol{\sigma} : \nabla \boldsymbol{u}_s$ scales with $T^{3/2}$ are plotted. Dashed line: equation (3.15). (*b*) Data in the low T regime where $-\boldsymbol{\sigma} : \nabla \boldsymbol{u}_s$ scales with T^2 are plotted. Dashed line: equation (3.22).

Before we move on to the low T regime, one can further improve the model accuracy by including a term that linearly depends on $\nabla \cdot \boldsymbol{u}_s$. Specifically, we have the following expression for the rate of dissipation J_{coll}:

$$J_{coll} = J_0 + J_u(\nabla \cdot \boldsymbol{u}_s). \tag{3.17}$$

We triple binned $(-\sigma_s : \nabla u_s)$ (which is assumed to balance with the rate of dissipation) with ϕ, T and $\nabla \cdot u_s$. To evaluate and model the terms J_0 and J_u, from the triple-binned data gathered above, for each combination of ϕ and T, we calculate the intercept (to obtain J_0) and slope (to obtain J_u) of $(-\sigma_s : \nabla u_s)$ versus $(\nabla \cdot u_s)$.

We can keep the same expression as in (3.15) for J_0. As shown in figure 10(*a*), the data from different granular temperatures collapse onto a curve that is captured by the
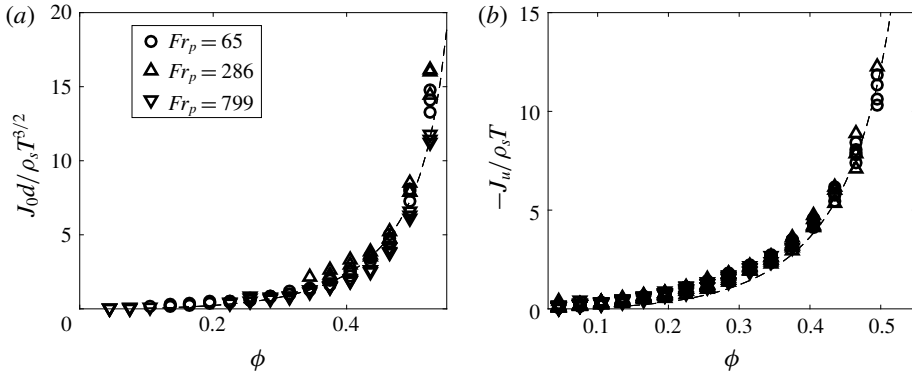
FIGURE 10. Rescaled J_0 (a) or rescaled J_u (b) is plotted against solid volume fraction for different granular temperatures and different Froude numbers. To obtain these values, we calculate the intercept (to obtain J_0) and slope (to obtain J_u) of $(-\sigma_s : \nabla u_s)$ versus $(\nabla \cdot u_s)$. In (a), the dashed line is from equation (3.15). In (b), the dashed line is from equation (3.19), where $\alpha_{J_u} = 3.5$. Data from fluidization simulations of non-cohesive particles; $Fr_p = 65$; $\langle \phi \rangle = 0.3$.

dashed line, validating the model. Furthermore, this collapse and agreement with the model prediction are both achieved for different particle diameters (different Froude numbers in the legend).

For J_u, we write (Gidaspow 1994):

$$J_u = -3(1 - e_{eff}^2)\phi^2 \rho_s g_0 T. \tag{3.18}$$

To test out this expression, in a similar fashion as done for J_0, we rescale J_u by T, and plot against ϕ in figure 10(b). We see data collapse onto a curve, supporting the scaling with T in the expression. For the model to capture the collapse, it is found that a proportionality constant α_{J_u} of 3.5 is needed. As indicated by the dashed line in figure 10(b), this constant works for different solid volume fractions, granular temperatures and particle diameters (as indicated by Froude number Fr_p). Thus, we have the following

$$J_u = -3\alpha_{J_u}(1 - e_{eff}^2)\phi^2 \rho_s g_0 T, \tag{3.19}$$

where $\alpha_{J_u} = 3.5$.

Now, we can move on to the lower granular temperature region.

It is useful to express (3.15) as

$$J_{coll,MKT} = f_J(\phi)\rho_s T / \tau_{vis}, \tag{3.20}$$

where $\tau_{vis} = d^2 \rho_s / \mu_s$. In the high T regime, as discussed in §3.1.3 on definitions of μ_s, we have $\mu_s \sim \rho_s d\sqrt{T}$, and the expression returns back to the one in (3.15).

At low T regime, where $\mu_s \sim \rho_s T\sqrt{d/g}$, we then anticipate

$$J_{coll,g} = f_{J,g}(\phi)\frac{\rho_s T^2}{d^2}\sqrt{d/g}. \tag{3.21}$$

If this model is reasonable, the rate of production of PTE by shear in the low T regime, scaled as $-\sigma : \nabla u_s d^2 / \rho_s T^2 \sqrt{d/g}$, should only be a function of ϕ independent

of the Froude number of the particles used in the simulations. Figure 9(*b*) confirms that the data do collapse reasonably well, supporting the model form chosen in (3.21). The dashed line in this figure corresponds to

$$f_{J,g}(\phi) = \alpha_{J,g}\phi^2 g_0(1 - e_{eff}^2),$$ (3.22)

where $\alpha_{J,g} = 45$.

As in the case of shear viscosity, we bridge J_{coll} in the low and high T regimes via

$$J_{coll} = \min(J_{coll,g}, J_{coll,c}),$$ (3.23)

where

$$J_{coll,c} = J_0 + J_u(\nabla \cdot \boldsymbol{u_s}).$$ (3.24)

3.1.5. *Summary*

It is found that the results for non-cohesive particles in the high T regime obtained by post-processing CFD-DEM simulations agree well with the constitutive expressions afforded by the kinetic theory of granular materials, which have been modified to include the effect of inter-particle friction. These findings demonstrate the validity of the adopted methodology. The present computational approach has also revealed a low T regime, where the inter-particle collision time is determined by gravitational fall between collisions. Modifications to the kinetic-theory constitutive models are proposed to capture both the low and high T regimes. Table 2 includes a summary of the constitutive models for non-cohesive particles.

3.2. *Cohesive particles*

Fluidization simulations were performed including inter-particle van der Waals forces with two Hamaker constants (see table 1). The cohesion strength is characterized by the Bond number $Bo^* = F_{coh}^{max}/(m_p|\boldsymbol{g}|)$. Here, F_{coh}^{max} is the maximum cohesive force between two particles. From (2.9), for $s = s_{min}^R \ll d$, F_{coh}^{max} becomes:

$$F_{coh}^{max} = F_{vdw}(A^R, s_{min}^R) = \frac{A^R d}{24 s_{min}^R{}^2}.$$ (3.25)

Figure 11(*a,b*) shows solid volume fraction on the *y*–*z* plane for non-cohesive and high cohesive cases, respectively. As expected, the cohesive case shows larger clusters compared with the non-cohesive case. It is also seen that there is a more uniform distribution of particles at moderate and high solid volume fractions.

3.2.1. *Pressure*

It is known from previous studies (Rognon *et al.* 2008; Gu *et al.* 2014; Irani *et al.* 2014) that cohesion bifurcates the inertial regime into two regimes: a new rate-independent regime (namely cohesive regime) at low shear rates and an inertial regime at high shear rates, where Bagnold scaling is observed and cohesion has little influence. The present CFD-DEM simulations reveal both of these regimes, as shown in figure 12. We also determined the average coordination number Z, defined as the average number of contacts per particle in each cell, and binned the results with ϕ and T, as illustrated in figure 13. Two trends which have been reported previously

$$\boldsymbol{\sigma} = [p - \mu_b(\boldsymbol{\nabla} \cdot \boldsymbol{u}_s)]\boldsymbol{I} - 2\mu_s\boldsymbol{S},$$

$$\boldsymbol{S} = \tfrac{1}{2}[\boldsymbol{\nabla}\boldsymbol{u}_s + (\boldsymbol{\nabla}\boldsymbol{u}_s)^{\mathrm{T}}] - \tfrac{1}{3}(\boldsymbol{\nabla} \cdot \boldsymbol{u}_s)\boldsymbol{I}.$$

$$g_0 = \frac{1 - \phi/2}{(1 - \phi)^3} + \frac{\alpha_{g_0}\phi^2}{(\phi_c - \phi)^{3/2}}.$$

$$\eta = (1 + e_p)/2, \quad e_{\mathit{eff}} = e_p - \tfrac{3}{2}\mu\exp(-3\mu).$$

Non-cohesive particles

$$p = \rho_s\phi[1 + 4\eta\phi g_0]T$$

$$\mu_b = \begin{cases} \alpha_{\mu_b,com}\eta\dfrac{8}{3\sqrt{\pi}}\phi^2 g_0\rho_s d\sqrt{T} & \text{for } \boldsymbol{\nabla} \cdot \boldsymbol{u}_s < 0, \\[3mm] \alpha_{\mu_b,dil}\eta\dfrac{8}{3\sqrt{\pi}}\phi^2 g_0\rho_s d\sqrt{T} & \text{for } \boldsymbol{\nabla} \cdot \boldsymbol{u}_s \geqslant 0. \end{cases}$$

$$\mu_s = \min(\mu_{s,g}, \mu_{s,c})$$

$$\mu_{s,g} = \alpha_{\mu_s,g}g_0\phi^2\rho_s T\sqrt{d/g}$$

$$\mu_{s,c} = \left(\frac{2 + \alpha_0}{6}\right)\left[\frac{5\sqrt{\pi}}{48 g_0\eta(2 - \eta)}\left(1 + \frac{8}{5}\phi\eta g_0\right)\left(1 + \frac{8}{5}\eta(3\eta - 2)\phi g_0\right) + \frac{16}{5}\eta\frac{\phi^2 g_0}{\sqrt{\pi}}\right]\rho_s d\sqrt{T}.$$

Pseudo-thermal energy balance: $-\boldsymbol{\sigma} : \boldsymbol{\nabla}\boldsymbol{u}_s = \min(J_{coll,g}, J_{coll,c})$;

$$J_{coll,g} = \alpha_{J,g}\phi^2 g_0(1 - e_{\mathit{eff}}{}^2)\frac{\rho_s T^2}{d^2}\sqrt{d/g}; \quad J_{coll,c} = J_0 + J_u(\boldsymbol{\nabla} \cdot \boldsymbol{u}_s);$$

$$J_0 = \frac{12}{\sqrt{\pi}}\phi^2 g_0(1 - e_{\mathit{eff}}{}^2)\frac{\rho_s T^{3/2}}{d}; \quad J_u = -3\alpha_{J_u}(1 - e_{\mathit{eff}}^2)\phi^2\rho_s g_0 T$$

Cohesive particles

$$F_{coh}^{max} = \frac{A^R d}{24 s_{min}^R{}^2}.$$

$$p = \begin{cases} \rho_s\phi[1 + 2(1 + e_p)\phi g_0]T - \alpha_{coh,1}\dfrac{F_{coh}^{max}}{d^2}\phi^2 & \text{for } \phi < \phi_a, \\[3mm] \rho_s\phi[1 + 2(1 + e_p)\phi g_0]T - \alpha_{coh,1}\dfrac{F_{coh}^{max}}{d^2}\phi^2 + \alpha_{coh,2}\dfrac{F_{coh}^{max}}{d^2}\dfrac{(\phi - \phi_a)^2}{(\phi_c - \phi)} & \text{for } \phi \geqslant \phi_a. \end{cases}$$

μ_b is the same as non-cohesive particles.

$$\mu = \min(\mu_{s,g}, \mu_{s,c}) + \frac{\tau_y}{\dot{\gamma}}\frac{W\left(\alpha_W\dfrac{\rho_s T}{\tau_y}\right)}{\alpha_W\dfrac{\rho_s T}{\tau_y}},$$

τ_y is yield stress, and $\tau_y = \dfrac{F_{coh}^{max}}{d^2}\dfrac{f_\phi(\phi)}{\phi_c - \phi}$, $f_\phi(\phi) = \phi(0.0249\phi^3 - 0.0215\phi^2 + 0.0048\phi + 0.0005)$

$$\dot{\gamma} = \sqrt{2\boldsymbol{S} : \boldsymbol{S}}$$

Pseudo-thermal energy balance:

$$-\boldsymbol{\sigma} : \boldsymbol{\nabla}\boldsymbol{u}_s = \min(J_{coll,g}(e_{coh}), J_{coll,c}(e_{coh})) + \alpha_{coh,3}\tau_y\frac{W\left(\alpha_W\dfrac{\rho_s T}{\tau_y}\right)}{\alpha_W\dfrac{\rho_s T}{\tau_y}}\frac{\sqrt{T}}{d}$$

$$e_{coh} = \sqrt{e_{\mathit{eff}}^2 - \frac{\alpha_e F_{coh}^{max} d}{mT}}.$$

Model parameters (for $\mu = 0.5$ and $e_p = 0.9$)

$\phi_c = 0.61$, $\alpha_{g_0} = 0.58$, $\alpha_{\mu_b,com} = 1.5$, $\alpha_{\mu_b,dil} = 1$, $\alpha_{\mu_s,g} = 8.0$, $\alpha_0 = 1.6$, $\alpha_{J_u} = 3.5$, $\alpha_{J,g} = 45$, $\alpha_{coh,1} = 3 \times 10^{-3}$, $\alpha_{coh,2} = 3.4 \times 10^{-3}$, $\phi_a = 0.2$, $\alpha_W = 14$, $\alpha_{coh,3} = 1.2$, $\alpha_e = 1 \times 10^{-7}$.

TABLE 2. Computationally generated kinetic-theory-based models for non-cohesive and cohesive particles proposed in the present study.
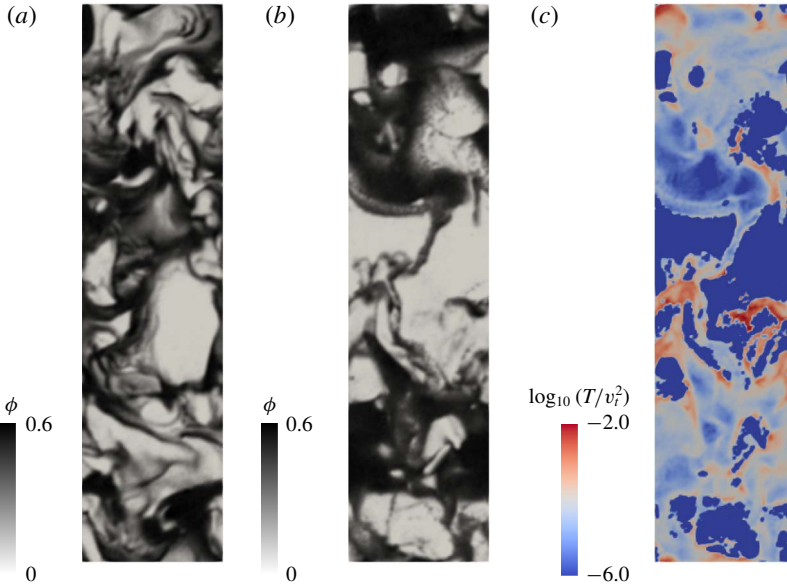
FIGURE 11. (Colour online) Snapshots of solid volume fraction for (*a*) non-cohesive, (*b*) high cohesive cases and (*c*) local granular temperature for high cohesive case. $Fr_p = 75$. Domain-averaged volume fraction $\langle \phi \rangle = 0.3$.
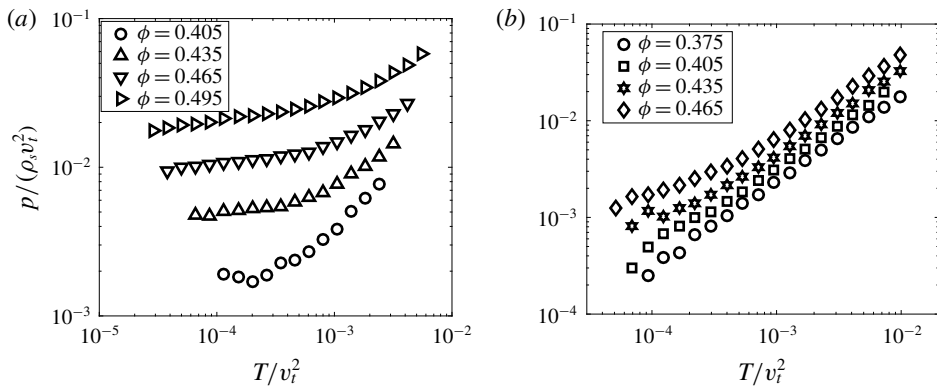

FIGURE 12. Dimensionless pressure versus dimensionless granular temperature for various particle volume fractions. Data from fluidization simulations of cohesive particles; $Bo^* = 960$ in (*a*) and $Bo^* = 96$ in (*b*); $Fr_p = 65$; $\langle \phi \rangle = 0.3$.

for cohesive particles (Rognon *et al.* 2008; Gu *et al.* 2014; Irani *et al.* 2014) are observed. First, at low T, Z increases with ϕ and plateaus at high ϕ values. Second, at a given ϕ, increasing T lowers Z, which is indicative of the disruption of the particle contact network. This consistency in the regime transition with the previous studies manifested in both a macroscopic quantity (p) and the microstructure (Z) again affirms the validity of the methodology in this study.
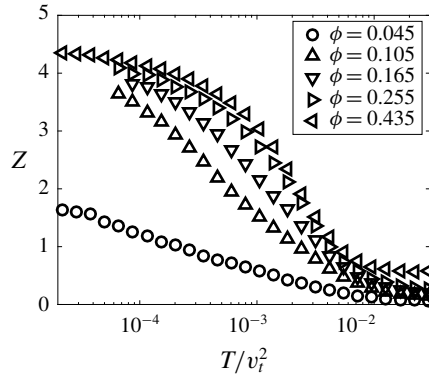
FIGURE 13. Average coordination number versus dimensionless granular temperature for various particle volume fractions. Data from fluidization simulations of cohesive particles; $Bo^* = 960$; $Fr_p = 65$; $\langle \phi \rangle = 0.3$.
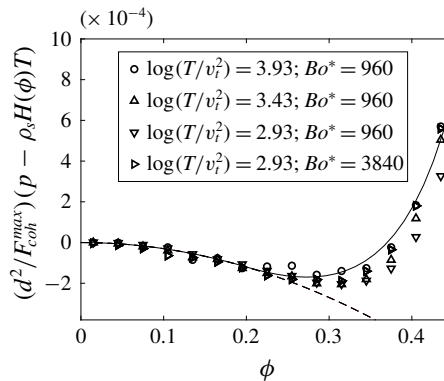

FIGURE 14. Scaled pressure contributed from cohesion versus local particle volume fraction. Solid line: equation (3.26). Data from fluidization simulations of cohesive particles; $Fr_p = 65$; $\langle \phi \rangle = 0.3$. Dashed line: equation (3.27).

However, different from these previous studies of cohesive particles (Rognon *et al.* 2008; Gu *et al.* 2014; Irani *et al.* 2014), the present methodology explores easily a wider parameter space; e.g. lower particle volume fractions in the low T temperature regime, which have been difficult to access (Gu *et al.* 2014; Irani *et al.* 2014). The results for this region are shown in figure 14. In this figure, to study the effects of cohesion, we subtract the contribution from collisions that are present for non-cohesive particles $\rho_s H(\phi)T$ from the total pressure p. We focus on the low temperature region where pressure is essentially temperature independent. One can see that, as ϕ increases, $p - \rho_s H(\phi)T$ starting from 0 initially decreases to become negative, and then increases.

This non-monotonic behaviour in the low temperature region can be understood physically as the following. In the low temperature region, effects from cohesion dominate over particle agitation. These effects from cohesion are manifested differently depending on the number of particles present locally. At low particle volume fractions ($\phi < 0.2$), where there are not enough particles to form force chains

that can transmit stress over large distances (low Z in figure 13), the attractive van der Waals interaction between particles decreases the pressure. At high particle volume fractions ($\phi > 0.2$), where the particles tend to form force chains (high Z in figure 13), the pressure increases.

We model this non-monotonic behaviour manifested by $p - \rho_s H(\phi)T$ in the low temperature region as follows. At low particle volume fraction, where attractive pair interaction is the principal correction, we write:

$$\frac{d^2}{F_{coh}^{max}}(p - \rho_s H(\phi)T) = -\alpha_{coh,1}\phi^2 \quad \text{for } \phi < \phi_a. \tag{3.26}$$

Here, $\phi_a = 0.2$ and $\alpha_{coh,1} = 3 \times 10^{-3}$. As shown in figure 14, this equation, denoted by a solid line, captures the data for $\phi < 0.2$. At high particle volume fraction, to capture the increase of pressure due to the force chains, we add a new term that is consistent with a previous study (Gu *et al.* 2014) on the right-hand side:

$$\frac{d^2}{F_{coh}^{max}}(p - \rho_s H(\phi)T) = -\alpha_{coh,1}\phi^2 + \alpha_{coh,2}\frac{(\phi - \phi_a)^2}{\phi_c - \phi} \quad \text{for } \phi \geqslant \phi_a. \tag{3.27}$$

Here, $\alpha_{coh,2} = 3.4 \times 10^{-3}$. As shown in figure 14, this equation, denoted by a dashed line, captures the data for $\phi > 0.2$.

Assembling these models together, we obtain the following:

$$p = \begin{cases} \rho_s\phi[1 + 2(1 + e_p)\phi g_0]T - \alpha_{coh,1}\dfrac{F_{coh}^{max}}{d^2}\phi^2 & \text{for } \phi < \phi_a \\[3mm] \rho_s\phi[1 + 2(1 + e_p)\phi g_0]T - \alpha_{coh,1}\dfrac{F_{coh}^{max}}{d^2}\phi^2 + \alpha_{coh,2}\dfrac{F_{coh}^{max}}{d^2}\dfrac{(\phi - \phi_a)^2}{(\phi_c - \phi)} & \text{for } \phi \geqslant \phi_a, \end{cases} \tag{3.28}$$

where $\alpha_{coh,1} = 3 \times 10^{-3}$, $\alpha_{coh,2} = 3.4 \times 10^{-3}$, $\phi_a = 0.2$ and $\phi_c = 0.61$.

For bulk viscosity, it is found that the inclusion of cohesion has a negligible impact on the values, and thus (3.8) is applied.

3.2.2. *Shear viscosity*

Figure 15(a–c) displays the variation of dimensionless shear stress ($\tau \equiv \mu_s\dot{\gamma}$, $\dot{\gamma} \equiv \sqrt{2\boldsymbol{S} : \boldsymbol{S}}$) with dimensionless granular temperature at different particle volume fractions, for both non-cohesive (a) and cohesive particles (b–c). Similar to pressure, shear stress is largely unaffected by cohesion in the high T regime, but becomes temperature independent in the low T limit. This behaviour is consistent with previous findings (Gu *et al.* 2014; Irani *et al.* 2014).

Figure 11(c) shows granular temperature in the y–z plane for the high cohesive case. Comparing figures 11(b) and 11(c) one can see that for high solid volume regions (clusters in the figure), the particles at boundary tend to have higher T and thus in inertial regime. Particles inside the clusters tend to have lower T and stay in cohesive regime.

The dip in the shear stress observed at the transition between these two regimes can readily be attributed to the destruction of force chains (as evidenced by a sharp decrease in Z) by increased particle agitation. To study this dip and the low temperature region, we examine in figure 16(a) the excess shear stress, defined as the
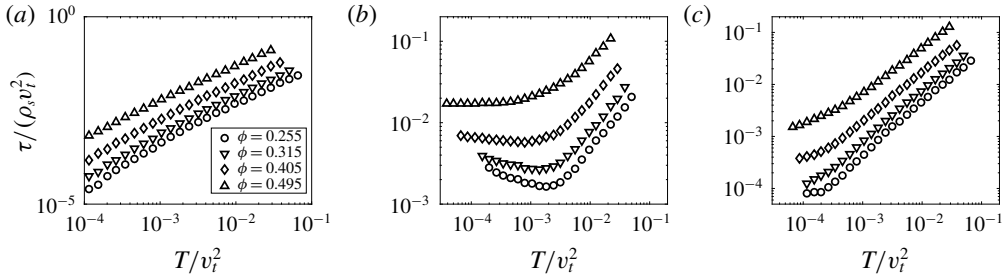
FIGURE 15. Dimensionless shear stress versus dimensionless granular temperature for various particle volume fractions. Data from fluidization simulations of both (a) non-cohesive particles and (b,c) cohesive particles; $Bo^* = 960$ in (b) and $Bo^* = 96$ in (c); $Fr_p = 65$; $\langle\phi\rangle = 0.3$.
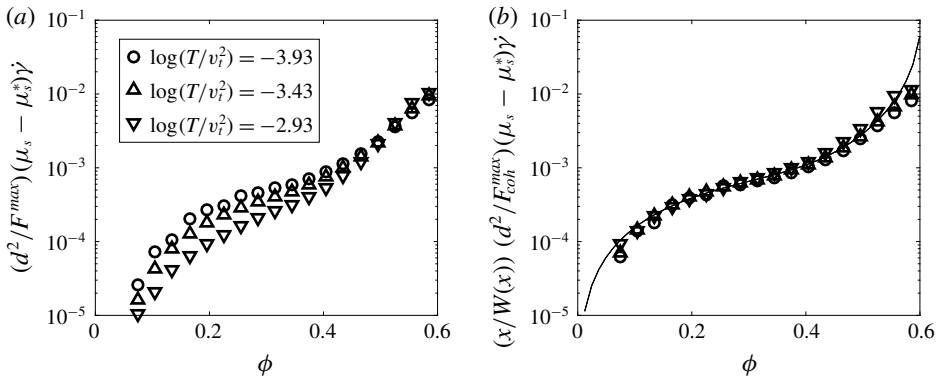

FIGURE 16. The variation of scaled excess shear stress with local particle volume fraction at different scaled granular temperatures. Data from fluidization simulations of cohesive particles; $Bo^* = 960$; $Fr_p = 65$; $\langle\phi\rangle = 0.3$. Data from (a) are rescaled in (b) through $x/W(x)$, where $x = \alpha_W(\rho_s T/\tau_y)$. Solid line in (b): equation (3.31).

difference in the shear stress in a cohesive system and a corresponding non-cohesive system. Specifically, we plot $(d^2/F_{coh}^{max})(\mu_s - \mu_s^*)\dot\gamma$, where $\mu_s^* = \min(\mu_{s,g}, \mu_{s,c})$ and μ_s denote viscosities of non-cohesive and cohesive systems, respectively. In order to capture the residual dependence on granular temperature, we adopt the model of Irani *et al.* (2014) based on the fluidity approach of Picard *et al.* (2002),

$$\mu\dot\gamma = \mu_s^*\dot\gamma + \tau_y\frac{W(x)}{x}. \quad (3.29)$$

Here, τ_y is the yield stress; $W(x)$ is the Lambert–W function, which is defined as $W^{-1}(z) = z\exp(z)$. For computation, its principal branch $(x > 0)$ can be approximated (Winitzki 2003) as $W(x) \approx [2\ln(1 + 0.8842y) - \ln(1 + 0.9294\ln(1 + 0.5106y)) - 1.213]/[1 + 1/(2\ln(1 + 0.8842y) + 4.688)]$, where $y = \sqrt{2ex + 2}$. Here, e is Napier's constant. As detailed by Irani *et al.* (2014), $W(x)/x$ captures the competition between kinetic energy supplied by shear and the cohesive energy. Correspondingly, we set $x = f_1(\phi)\rho_s T d^2/F_{coh}^{max}$. Similar to the expression for pressure, the yield stress τ_y has the form $\tau_y = f_2(\phi)F_{coh}^{max}/d^2$.

Thus, (3.29) becomes,

$$f_2(\phi) = \frac{d^2}{F_{coh}^{max}} \frac{f_1(\phi)\dfrac{\rho_s T d^2}{F_{coh}^{max}}}{W\left(f_1(\phi)\dfrac{\rho_s T d^2}{F_{coh}^{max}}\right)}(\mu\dot{\gamma} - \mu^*\dot{\gamma}). \tag{3.30}$$

We find $f_1(\phi)$ and $f_2(\phi)$ as follows: at various chosen ϕ values, we demand that equation (3.30) be satisfied at two temperatures. Such an analysis leads to us conclude that $f_1(\phi)$ and $1/f_2(\phi)$ have essentially the same ϕ dependence. Therefore, $x = f_1(\phi)\rho_s T d^2/F_{coh}^{max} \sim (1/f_2(\phi))(\rho_s T d^2/F_{coh}^{max}) \sim \rho_s T/\tau_y$. Within the framework of the computationally deduced model, the ϕ dependence of τ_y as denoted by $f_2(\phi)$ is simply correlated as

$$\tau_y = \frac{f_\phi(\phi)}{\phi_c - \phi} \frac{F_{coh}^{max}}{d^2}, \tag{3.31}$$

where $f_\phi(\phi) = \phi(0.0249\phi^3 - 0.0215\phi^2 + 0.0048\phi + 0.0005)$. Correspondingly, $x = \alpha_W(\rho_s T/\tau_y)$, where $\alpha_W = 14$.

Using the $x/W(x)$ scaling from the fluidity approach where x is defined as above, the data points from different temperatures shown in figure 16(a) are now collapsed onto a single curve in (b). This collapse of data is captured by (3.31), as denoted by the solid line in the figure.

Thus, we have the final shear viscosity model for cohesive particles:

$$\mu = \mu_s^* + \frac{\tau_y}{\dot{\gamma}} \frac{W\left(\alpha_W \dfrac{\rho_s T}{\tau_y}\right)}{\alpha_W \dfrac{\rho_s T}{\tau_y}}. \tag{3.32}$$

It should be noted that this yield-stress-based model for cohesive particles is consistent with prior observations from both experiments and simulations. For fluidization of Geldart Group A particles (Geldart 1973), for which inter-particle van der Waals forces start to become important compared to particle weight, a bubbleless expanded regime is observed in both experiments (Geldart 1973; Menon & Durian 1997) and simulations (Hou, Zhou & Yu 2012; Gu *et al.* 2016b). Both experiments (Geldart 1973; Menon & Durian 1997) and simulations (Hou *et al.* 2012; Gu *et al.* 2016b) found that particles are essentially in a static state in this regime. This regime corresponds to the case where the shear stress supplied in the system does not overcome the yield stress τ_y. Furthermore, it has been found in these experimental and simulation studies that the formation of this regime depends on particle volume fraction of the system, which is consistent with the dependence of τ_y on particle volume fraction ϕ.

3.2.3. *Pseudo-thermal energy balance*

Similar to the analysis on non-cohesive particles, figure 17 shows the variation of $(-\boldsymbol{\sigma}:\nabla\boldsymbol{u}_s)$ with temperature at three different volume fractions. At high T, cohesion has little effect. However, the cohesive systems differ noticeably from the non-cohesive case at low temperatures; this behaviour can be explained by two hypotheses: (i) the part of $(-\boldsymbol{\sigma}:\nabla\boldsymbol{u}_s)$ associated with cohesive yield stress is not a source of PTE or
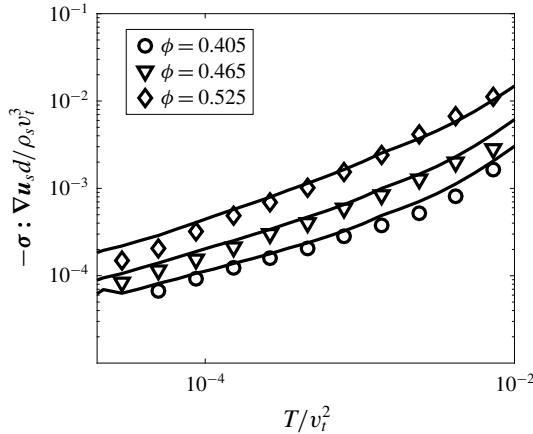
FIGURE 17. Dimensionless rate of production of PTE by shear versus dimensionless granular temperature for various particle volume fractions. Data from fluidization simulations of cohesive particles; rate of production of PTE is triple binned by particle volume fraction, granular temperature and rate of dilation. The data are then processed by conditioning on the rate of dilation being zero, and plotted here for; $Bo^* = 960$; $Fr_p = 65$; $\langle \phi \rangle = 0.3$. Solid lines: equations (3.24) (3.21) (3.34).

(ii) there is an additional rate of PTE dissipation associated with the cohesive yield stress. There is precedence in the literature for the first argument. For example, in frictional–kinetic models, only the kinetic part of the stress is recognized as a source in the PTE balance in a number of studies (Ocone, Sundaresan & Jackson 1993; Alam & Nott 1997; Srivastava & Sundaresan 2003). In this spirit, we identify $-\boldsymbol{\sigma} : \nabla \boldsymbol{u}_s - \dot{\gamma} \tau_y W(x)/x$ as the source of PTE.

Regarding the dissipation term of PTE by inter-particle collisions, cohesion is known (from both experiments (Kim & Dunn 2007) and simulations (Murphy & Subramaniam 2015; Gu *et al.* 2016*a*; Kellogg *et al.* 2017)) to alter the effective restitution coefficient for a two-particle collision. When two cohesive particles undergo a head-on collision, the effective restitution coefficient goes to zero as the impact velocity drops below some critical value; the effective restitution coefficient approaches the non-cohesive limit at high impact velocities. Based on energy balance, a relation has been derived and verified with particle–surface collision experiments (Kim & Dunn 2007; Gu *et al.* 2016*a*) to connect the effective restitution coefficient for cohesive particles e_{coh} to the one for non-cohesive particles e_{eff} (accounting for inelasticity and friction only). Replacing the impact velocity v_{impact} with granular temperature T as $T = v_{impact}^2$, we have the following relation

$$e_{coh} = \sqrt{e_{eff}^2 - \frac{\alpha_e F_{coh}^{max} d}{mT}}. \tag{3.33}$$

PTE balance now becomes

$$-\boldsymbol{\sigma} : \nabla \boldsymbol{u}_s - \dot{\gamma} \tau_y W(x)/x = \min(J_{coll,g}(e_{coh}), J_{coll,c}(e_{coh})), \tag{3.34}$$

where α_e is fit to be 1×10^{-7}. As shown in figure 17, this equation captures all the regimes as well as the transitions between them.

3.2.4. *Summary*

Analysis of the results obtained with cohesive particles reveals the following. First, the cohesion introduces a correction to the pressure, which could be non-negligible at low T values. Second, the cohesive system manifests a yield stress, whose decreasing strength with increasing particle agitation can be quantified via the fluidity approach. Third, cohesive interaction lowers the effective coefficient of restitution in a T-dependent fashion that is easily rationalized based on two-particle collision studies. Table 2 includes a summary of the proposed closure models.

4. Summary

In this paper, we have formulated constitutive models for particle phase stress based on CFD-DEM simulations of gas-fluidized beds of non-cohesive and mildly cohesive (Geldart Group A) particles. Based on the simulation results, closures for pressure, bulk viscosity, shear viscosity and the rate of dissipation of the pseudo-thermal energy are proposed.

For non-cohesive particles, the present results are consistent with analytically derived kinetic-theory models in the high T limit, confirming their validity. In addition, the present study has uncovered a low T regime where the closures manifest different scalings and a definite dependence on gravitational acceleration.

Particles interacting through van der Waals force are then studied as a model cohesive system. Cohesion has little effect on pressure in the high T regime. In the low T regime, it lowers the pressure at low particle volume fractions and increases it at higher volume fractions when force chains begin to form. Cohesive systems subjected to shear manifest yield stress, whose strength increases rapidly with particle volume fraction. Interestingly, the results suggest that particle agitation lowers the effective yield stress; this weakening of the yield-stress contribution is readily accounted for in the model via the fluidity approach described previously in the literature (Picard *et al.* 2002; Irani *et al.* 2014).

The main motivation of this study is to investigate fluidization characteristics of mildly cohesive particles and how inter-play between cohesion and interstitial fluid alters mesostructures of flow and solid phase stresses. A powerful approach to modelling gas–particle flows with dynamic agglomerates is to use a population balance model coupled with Eulerian transport equations (see e.g. Marchisio, Vigil & Fox (2003), Marchisio & Fox (2013), Kellogg *et al.* (2017)). In mildly cohesive systems, for example fluidization of cohesive Geldart Group A particles, a simpler approach that incorporates the effects of cohesion into stress models directly without solving an additional population balance is attractive. Previous studies such as those of Arastoopour (2001), Kim & Arastoopour (2002), Seu-Kim & Arastoopour (1995), extended the standard kinetic theory of granular materials to simulate cohesive particles. In these studies and herein, we show how one can still retain the framework of the kinetic theory of granular materials to evolve the granular temperature in particulate flows, but modify it in a simple fashion to account for cohesion. This opens up the possibility of simulating fluidization behaviour of mildly cohesive (Geldart Group A (Geldart 1973)) particles using the kinetic-theory framework, which is widely used to simulate fluidization of non-cohesive (Geldart Group B) particles.

In this study, we considered only gas–solid flows in unbounded domains and showed that the assumption of local equilibrium of granular temperature is valid to a very good approximation. However, the presence of wall boundaries further complicates the flow behaviour and not only alters macroscale structures but also it
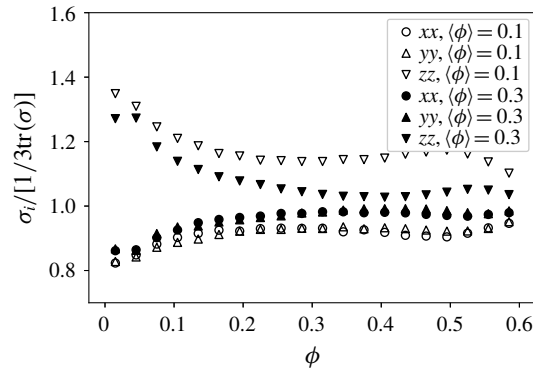
FIGURE 18. Normal stress components scaled by the trace of the stress versus particle volume fraction. The results are based on data from fluidization simulations of non-cohesive particles with $Fr_p = 65$ performed for different domain-averaged particle volume fractions.

causes production, destruction and redistribution of the granular temperature. Effects of wall boundaries on the constitutive relations are beyond the scope of this study and should be investigated in further studies.

The present approach can be applied to particles interacting through complex inter-particle forces, such as the liquid-bridge force when the particles are wet and the electrostatic force when the particles carry charges.

Acknowledgement

Appendix A.

Figure 18 plots scaled normal stress components $\sigma_i/(1/3\mathrm{tr}(\boldsymbol{\sigma}))$ against particle volume fraction ϕ. The data are from fluidization simulations of non-cohesive particles with $Fr_p = 65$. Horizontal normal stress components σ_{xx} and σ_{yy} are indistinguishable, to within computational accuracy. At higher volume fractions, the variation of stress is under $\pm 20\%$. As volume fraction decreases, the anisotropy increases. This behaviour is expected as there are fewer collisions at lower volume fractions.

Appendix B. Effect of microscopic drag law on constitutive relations

To study the effects of the microscopic drag law on the constitutive relations, we performed an additional simulation with Beetstra's drag law (Beetstra, van der Hoef & Kuipers 2007). In this simulation, the domain size is $180d_p \times 180d_p \times 720d_p$ with a particle diameter of $145\,\mu$m and domain-averaged solid volume fraction $\langle\phi\rangle$ of 0.1. We generated figure 3(b) (scaled solid pressure versus solid volume fraction) of the manuscript and the scaled solid shear viscosity versus scaled granular temperature for Beetstra's drag law, which is shown in figure 19. These figures show that the dependency of solid pressure and shear viscosity is essentially independent of choice of the microscopic drag law.
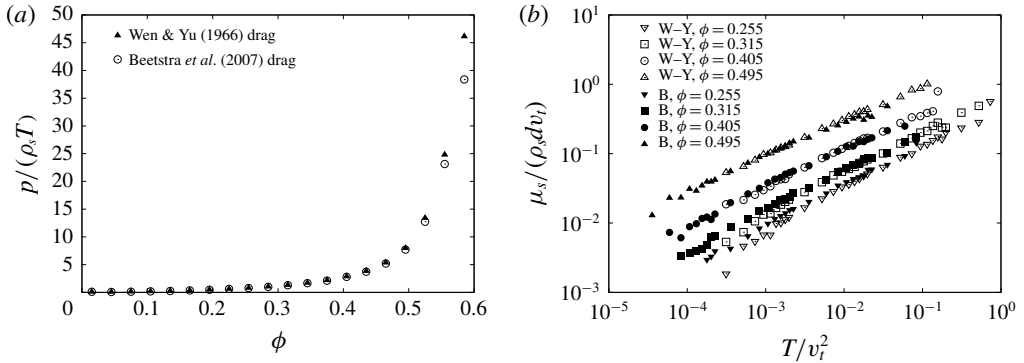
FIGURE 19. (*a*) Pressure scaled by granular temperature versus local particle volume fraction and (*b*) shear viscosity versus granular temperature for the Wen & Yu (1966) and Beetstra *et al.* (2007) drag laws. In the legend, W–Y and B denote Wen & Yu and Beetstra drag laws, respectively. Particle diameters d_p are 75 µm and 145 µm for Wen & Yu and Beetstra *et al.* cases, respectively. Domain-averaged solid volume fraction $\langle \phi \rangle = 0.1$.

Changing the drag law can alter the details of the mesoscale structure and the prevailing granular temperature; however, as is clear from the comparison we show here, the drag law does not have any systematic effect on the relationship between particle phase viscosity and granular temperature. In other words, in our simulations, the fluid–particle drag principally supplies energy to sustain the fluctuating motion of the particles in this dissipative system.

Appendix C. Effect of mapping mesh size on constitutive relations

The computed Eulerian particle velocity $\boldsymbol{u}_s$ and granular temperature T are dependent on the mapping mesh size selection. To study the mesh dependency of these variables, we mapped particle velocity and solid volume fraction on a mesh size of $4d_p$ and $5d_p$. It is worth remembering that the mesh size and the CFD grid size are $3d_p$ in our reference case. Figure 20 shows the scaled solid pressure versus solid volume fraction for various mapping cell sizes. The discrepancy from Lun *et al.* (1984) increases as the mapping mesh size increases. It is expected that, with larger mesh size, we account for inhomogeneities from averaging whereas the kinetic theory uses the assumption of homogeneous distribution of particles in a control volume.

Capecelatro *et al.* (2015) stated that computed statistics, such as particle fluctuating energy, were independent of the number of particles if the number of particles inside a cell volume is greater than 10. We have checked the number of particles in a cell volume in the range of volume fractions ($0.1 < \phi < 0.6$) that we have studied. As an example, we have approximately 10 particles inside the filtering volume with the smallest cell size of $\Delta = 3d_p$ at the filtered solid volume fraction $\phi = 0.2$ which should give adequate statistics.

Appendix D. Number of realizations of macroscopic quantities

Figure 21 shows how frequently local variables of granular temperature and particle volume fraction take different values. The numbers in this figure are per snapshot, and
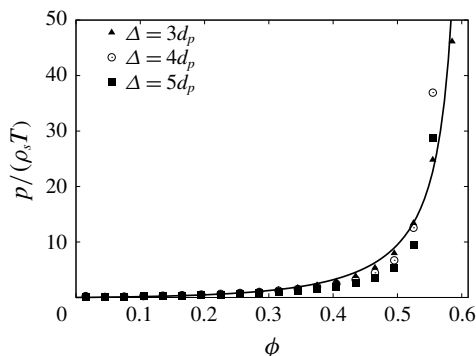
FIGURE 20. Pressure scaled by granular temperature versus particle volume fraction for various mapping mesh sizes. $Fr_p = 65$; $\langle \phi \rangle = 0.1$.
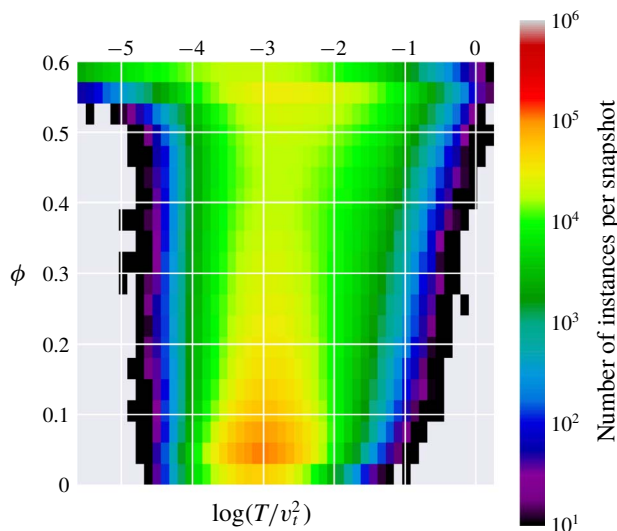

FIGURE 21. (Colour online) Collection of statistics for a given local granular temperature and local particle volume fraction, based on data from a single snapshot. Non-cohesive particles with $Fr_p = 65$ and $\langle \phi \rangle = 0.3$.

we typically use data from more than eight snapshots. As exemplified in the figure, all analyses in the manuscript are based on a parameter space where enough statistics have been collected, as one can confirm by comparing the figure here with other figures in the manuscript; specifically, in each bin (characterized by a set of ϕ and T) from which the result is averaged, we have collected over $\sim$100 data points.

REFERENCES

AARONS, L. & SUNDARESAN, S. 2006 Shear flow of assemblies of cohesive and non-cohesive granular materials. *Powder Technol.* **169** (1), 10–21.

AGRAWAL, K., LOEZOS, P. N., SYAMLAL, M. & SUNDARESAN, S. 2001 The role of meso-scale structures in rapid gas–solid flows. *J. Fluid Mech.* **445**, 151–185.

ALAM, M. & NOTT, P. R. 1997 The influence of friction on the stability of unbounded granular shear flow. *J. Fluid Mech.* **343**, 267–301.

ARASTOOPOUR, H. 2001 Numerical simulation and experimental analysis of gas/solid flow systems: 1999 Fluor-Daniel Plenary lecture. *Powder Technol.* **119** (2–3), 59–67.

BALZER, G., BOËLLE, A. & SIMONIN, O. 1995 Fluidized, Eulerian gas–solid flow modelling of dense fluidized beds. In *Fluidization VIII*, p. 1125.

BEETSTRA, R., VAN DER HOEF, M. A. & KUIPERS, J. A. M. 2007 Drag force of intermediate reynolds number flow past mono- and bidisperse arrays of spheres. *AIChE J.* **53** (2), 489–501.

BERZI, D. & VESCOVI, D. 2015 Different singularities in the functions of extended kinetic theory at the origin of the yield stress in granular flows. *Phys. Fluids* **27** (1), 013302.

BOËLLE, A., BALZER, G. & SIMONIN, O. 1995 Second-order prediction of the particle-phase stress tensor of inelastic spheres in simple shear dense suspensions. In *Proceedings of the 6th International Symposium on Gas–Solid Flows, ASME FED*, vol. 228, pp. 9–18.

BOYCE, C. M., OZEL, A., KOLEHMAINEN, J. & SUNDARESAN, S. 2017 Analysis of the effect of small amounts of liquid on gas–solid fluidization using CFD-DEM simulations. *AIChE J.* **63** (12), 1547–5905.

CAMPBELL, C. S. 2002 Granular shear flows at the elastic limit. *J. Fluid Mech.* **465**, 261–291.

CAPECELATRO, J., DESJARDINS, O. & FOX, R. O. 2014 Numerical study of collisional particle dynamics in cluster-induced turbulence. *J. Fluid Mech.* **747**, R2.

CAPECELATRO, J., DESJARDINS, O. & FOX, R. O. 2015 On fluid-particle dynamics in fully developed cluster-induced turbulence. *J. Fluid Mech.* **780**, 578–635.

CAPECELATRO, J., DESJARDINS, O. & FOX, R. O. 2016a Strongly coupled fluid-particle flows in vertical channels. I. Reynolds-averaged two-phase turbulence statistics. *Phys. Fluids* **28** (3), 033306.

CAPECELATRO, J., DESJARDINS, O. & FOX, R. O. 2016b Strongly coupled fluid-particle flows in vertical channels. II. Turbulence modeling. *Phys. Fluids* **28** (3), 033307.

CHIALVO, S., SUN, J. & SUNDARESAN, S. 2012 Bridging the rheology of granular flows in three regimes. *Phys. Rev.* E **85** (2), 021305.

CHIALVO, S. & SUNDARESAN, S. 2013 A modified kinetic theory for frictional granular flows in dense and dilute regimes. *Phys. Fluids* **25** (7), 070603.

DA CRUZ, F., EMAM, S., PROCHNOW, M., ROUX, J.-N. & CHEVOIR, F. 2005 Rheophysics of dense granular materials: discrete simulation of plane shear flows. *Phys. Rev.* E **72** (2), 21309.

CUNDALL, P. A. & STRACK, O. D. L. 1979 A discrete numerical model for granular assemblies. *Geotechnique* **29** (1), 47–65.

DERKSEN, J. J. & SUNDARESAN, S. 2007 Direct numerical simulations of dense suspensions: wave instabilities in liquid-fluidized beds. *J. Fluid Mech.* **587**, 303–336.

DOI, T., SANTOS, A. & TIJ, M. 1999 Numerical study of the influence of gravity on the heat conductivity on the basis of kinetic theory. *Phys. Fluids* **11** (11), 3553–3559.

FÉVRIER, P., SIMONIN, O. & SQUIRES, K. D. 2005 Partitioning of particle velocities in gas–solid turbulent flows into a continuous field and a spatially uncorrelated random distribution: theoretical formalism and numerical study. *J. Fluid Mech.* **533**, 1–46.

FORSYTH, A. J., HUTTON, S. & RHODES, M. J. 2002 Effect of cohesive interparticle force on the flow characteristics of granular material. *Powder Technol.* **126**, 150–154.

FOX, R. O. 2014 On multiphase turbulence models for collisional fluid-particle flows. *J. Fluid Mech.* **742**, 368–424.

GARZÓ, V. & DUFTY, J. W. 1999 Dense fluid transport for inelastic hard spheres. *Phys. Rev.* E **59** (5), 5895–5911.

GARZÓ, V., TENNETI, S., SUBRAMANIAM, S. & HRENYA, C. M. 2012 Enskog kinetic theory for monodisperse gas–solid flows. *J. Fluid Mech.* **712**, 129–168.

GELDART, D. 1973 Types of gas fluidization. *Powder Technol.* **7**, 285–292.

GIDASPOW, D. 1994 *Multiphase Flow and Fluidization: Continuum and Kinetic Theory Descriptions*. Academic Press.

GIDASPOW, D. & HUILIN, L. 1998 Equation of state and radial distribution functions of FCC particles in a CFB. *AIChE J.* **44** (2), 279–293.

GOLDSTEIN, D., HANDLER, R. & SIROVICH, L. 1993 Modeling a no-slip flow boundary with an external force field. *J. Comput. Phys.* **105** (2), 354–366.

GONIVA, C., KLOSS, C., DEEN, N. G., KUIPERS, J. A. M. & PIRKER, S. 2012 Influence of rolling friction on single spout fluidized bed simulation. *Particuology* **10** (5), 582–591.

GU, Y., CHIALVO, S. & SUNDARESAN, S. 2014 Rheology of cohesive granular materials across multiple dense-flow regimes. *Phys. Rev.* E **90** (3), 32206.

GU, Y., OZEL, A. & SUNDARESAN, S. 2016a A modified cohesion model for CFD-DEM simulations of fluidization. *Powder Technol.* **296**, 17–28.

GU, Y., OZEL, A. & SUNDARESAN, S. 2016b Numerical studies of the effects of fines on fluidization. *AIChE J.* **62** (7), 2271–2281.

GU, Y., OZEL, A. & SUNDARESAN, S. 2016c Rheology of granular materials with size distributions across dense-flow regimes. *Powder Technol.* **295**, 322–329.

HAMAKER, H. C. 1937 The London-van der Waals attraction between spherical particles. *Physica* **4** (10), 1058–1072.

HOU, Q. F., ZHOU, Z. Y. & YU, A. B. 2012 Micromechanical modeling and analysis of different flow regimes in gas fluidization. *Chem. Engng Sci.* **84**, 449–468.

IRANI, E., CHAUDHURI, P. & HEUSSINGER, C. 2014 Impact of attractive interactions on the rheology of dense athermal particles. *Phys. Rev. Lett.* **112** (18).

ISRAELACHVILI, J. N. 2010 *Intermolecular and Surface Forces*, 3rd edn. Academic Press.

JENKINS, J. T. & RICHMAN, M. W. 1985a Grad's 13-moment system for a dense gas of inelastic spheres. *Arch. Rat. Mech. Anal.* **87** (4).

JENKINS, J. T. & RICHMAN, M. W. 1985b Kinetic theory for plane flows of a dense gas of identical, rough, inelastic, circular disks. *Phys. Fluids* **28** (12), 3485–3494.

JENKINS, J. T. & SAVAGE, S. B. 1983 A theory for the rapid flow of identical, smooth, nearly elastic, spherical particles. *J. Fluid Mech.* **130**, 187–202.

JENKINS, J. T. & ZHANG, C. 2002 Kinetic theory for identical, frictional, nearly elastic spheres. *Phys. Fluids* **14** (3), 1228–1235.

JOHNSON, K. L. 1987 *Contact Mechanics*. Cambridge University Press.

JOP, P., FORTERRE, Y. & POULIQUEN, O. 2006 A constitutive law for dense granular flows. *Nature* **441**, 727–730.

KELLOGG, K. M., LIU, P., LAMARCHE, C. Q. & HRENYA, C. M. 2017 Continuum theory for rapid cohesive-particle flows: general balance equations and discrete-element-method-based closure of cohesion-specific quantities. *J. Fluid Mech.* **832**, 345–382.

KIM, H. & ARASTOOPOUR, H. 2002 Extension of kinetic theory to cohesive particle flow. *Powder Technol.* **122** (1), 83–94.

KIM, O. V. & DUNN, P. F. 2007 A microsphere-surface impact model for implementation in computational fluid dynamics. *J. Aerosol. Sci.* **38** (5), 532–549.

KLOSS, C., GONIVA, C., HAGER, A., AMBERGER, S. & PIRKER, S. 2012 Models, algorithms and validation for opensource DEM and CFD–DEM. *Prog. Comput. Fluid Dyn.* **12** (2), 140–152.

KOBAYASHI, T., TANAKA, T., SHIMADA, N. & KAWAGUCHI, T. 2013 DEM-CFD analysis of fluidization behavior of Geldart Group A particles using a dynamic adhesion force model. *Powder Technol.* **248**, 143–152.

KOCH, D. L. 1990 Kinetic theory for a monodisperse gas–solid suspension. *Phys. Fluids* A **2** (10), 1711.

KOCH, D. L. & SANGANI, A. S. 1999 Particle pressure and marginal stability limits for a homogeneous monodisperse gas-fluidized bed: kinetic theory and numerical simulations. *J. Fluid Mech.* **400**, 229–263.

KOLEHMAINEN, J., OZEL, A., BOYCE, C. M. & SUNDARESAN, S. 2016 A hybrid approach to computing electrostatic forces in fluidized beds of charged particles. *AIChE J.* **62** (7), 2282–2295.

KUMARAN, V. 2004 Constitutive relations and linear stability of a sheared granular flow. *J. Fluid Mech.* **506**, 1–43.

KUMARAN, V. 2006 The constitutive relation for the granular flow of rough particles, and its application to the flow down an inclined plane. *J. Fluid Mech.* **561**, 1–42.

KUWAGI, K., MIKAMI, T. & HORIO, M. 2000 Numerical simulation of metallic solid bridging particles in a fluidized bed at high temperature. *Powder Technol.* **109** (1–3), 27–40.

LIU, P., LAMARCHE, C. Q., KELLOGG, K. M. & HRENYA, C. M. 2016 Fine-particle defluidization: Interaction between cohesion, Youngs modulus and static bed height. *Chem. Engng Sci.* **145**, 266–278.

LUN, C. K. K. 1991 Kinetic theory for granular flow of dense, slightly inelastic, slightly rough spheres. *J. Fluid Mech.* **233**, 539–559.

LUN, C. K. K. & SAVAGE, S. B. 2003 Kinetic theory for inertia flows of dilute turbulent gas–solids mixtures. In *Granular Gas Dynamics* (ed. T. Pöschel & N. Brilliantov), pp. 267–289. Springer.

LUN, C. K. K., SAVAGE, S. B., JEFFREY, D. J. & CHEPURNIY, N. 1984 Kinetic theories for granular flow: inelastic particles in Couette flow and slightly inelastic particles in a general flowfield. *J. Fluid Mech.* **140**, 223–256.

MA, X. & KATO, K. 1998 Effect of interparticle adhesion forces on elutriation of fine powders from a fluidized bed of a binary particle mixture. *Powder Technol.* **95** (2), 93–101.

MARCHISIO, D. L. & FOX, R. O. 2013 *Computational Models for Polydisperse Particulate and Multiphase Systems*. Cambridge University Press.

MARCHISIO, D. L., VIGIL, R. D. & FOX, R. O. 2003 Quadrature method of moments for aggregation–breakage processes. *J. Colloid Interface Sci.* **258** (2), 322–334.

MAURIN, R., CHAUCHAT, J. & FREY, P. 2016 Dense granular flow rheology in turbulent bedload transport. *J. Fluid Mech.* **804**, 490–512.

MENON, N. & DURIAN, D. J. 1997 Particle motions in a gas-fluidized bed of sand. *Phys. Rev. Lett.* **79** (18), 3407–3410.

MIDI, G. D. R. 2004 On dense granular flows. *Eur. Phys. J.* E **14**, 341–365.

MOON, S. J., KEVREKIDIS, G. I. & SUNDARESAN, S. 2006 Compaction and dilation rate dependence of stresses in gas-fluidized beds. *Phys. Fluids* **18** (8), 083304.

MORENO-ATANASIO, R., XU, B. H. & GHADIRI, M. 2007 Computer simulation of the effect of contact stiffness and adhesion on the fluidization behaviour of powders. *Chem. Engng Sci.* **62** (1–2), 184–194.

MURPHY, E. & SUBRAMANIAM, S. 2015 Freely cooling granular gases with short-ranged attractive potentials. *Phys. Fluids* **27** (4), 043301.

MURPHY, E. & SUBRAMANIAM, S. 2017 Binary collision outcomes for inelastic soft-sphere models with cohesion. *Powder Technol.* **305**, 462–476.

OCONE, R., SUNDARESAN, S. & JACKSON, R. 1993 Gas–particle flow in a duct of arbitrary inclination with particle–particle interactions. *AIChE J.* **39** (8), 1261–1271.

OLSSON, P. & TEITEL, S. 2007 Critical scaling of shear viscosity at the jamming transition. *Phys. Rev. Lett.* **99** (17), 178001.

OPENCFD 2013 OpenFOAM 2.2.2 User Manual.

OTSUKI, M. & HAYAKAWA, H. 2009 Critical behaviors of sheared frictionless granular materials near the jamming transition. *Phys. Rev.* E **80**, 11308.

OZEL, A., GU, Y., MILIOLI, C. C., KOLEHMAINEN, J. & SUNDARESAN, S. 2017 Towards filtered drag force model for non-cohesive and cohesive particle-gas flows. *Phys. Fluids* **29** (10), 103308.

OZEL, A., KOLEHMAINEN, J., RADL, S. & SUNDARESAN, S. 2016 Fluid and particle coarsening of drag force for discrete-parcel approach. *Chem. Engng Sci.* **155**, 258–267.

PICARD, G., AJDARI, A., BOCQUET, L. & LEQUEUX, F. 2002 Simple model for heterogeneous flows of yield stress fluids. *Phys. Rev.* E **66** (5), 051501.

RENZO, A. D. & MAIO, F. P. D. 2004 Comparison of contact-force models for the simulation of collisions in DEM-based granular flow codes. *Chem. Engng Sci.* **59** (3), 525–541.

ROGNON, P. G., ROUX, J.-N., NAAÏM, M. & CHEVOIR, F. 2008 Dense flows of cohesive granular materials. *J. Fluid Mech.* **596**, 21–47.

ROGNON, P. G., ROUX, J.-N., NAAÏM, M. & CHEVOIR, F. 2007 Dense flows of bidisperse assemblies of disks down an inclined plane. *Phys. Fluids* **19** (5), 58101.

SAITOH, K., TAKADA, S. & HAYAKAWA, H. 2015 Hydrodynamic instabilities in shear flows of dry cohesive granular particles. *Soft Matt.* **11** (32), 6371–6385.

SELA, N. & GOLDHIRSCH, I. 1998 Hydrodynamic equations for rapid flows of smooth inelastic spheres, to Burnett order. *J. Fluid Mech.* **361**, 41–74.

SELA, N., GOLDHIRSCH, I. & NOSKOWICZ, S. H. 1996 Kinetic theoretical study of a simply sheared two-dimensional granular gas to Burnett order. *Phys. Fluids* **8** (9), 2337–2353.

SEU-KIM, H. & ARASTOOPOUR, H. 1995 Simulation of FCC particles flow behavior in a CFB using modified kinetic theory. *Can. J. Chem. Engng* **73** (5), 603–611.

SRIVASTAVA, A. & SUNDARESAN, S. 2003 Analysis of a frictional–kinetic model for gas–particle flow. *Powder Technol.* **129** (1–3), 72–85.

SUN, J. & SUNDARESAN, S. 2011 A constitutive model with microstructure evolution for flow of rate-independent granular materials. *J. Fluid Mech.* **682**, 590–616.

TAKADA, S., SAITOH, K. & HAYAKAWA, H. 2014 Simulation of cohesive fine powders under a plane shear. *Phys. Rev.* E **90** (6), 062207.

TAKADA, S., SAITOH, K. & HAYAKAWA, H. 2016 Kinetic theory for dilute cohesive granular gases with a square well potential. *Phys. Rev.* E **94** (1), 12906.

TRIPATHI, A. & KHAKHAR, D. V. 2011 Rheology of binary granular mixtures in the dense flow regime. *Phys. Fluids* **23** (11), 113302.

VAN WACHEM, B. & SASIC, S. 2008 Derivation, simulation and validation of a cohesive particle flow CFD model. *AIChE J.* **54** (1), 9–19.

WEN, C. Y. & YU, Y. H. 1966 Mechanics of fluidization. *Chem. Engng Prog.* **62** (62), 100–111.

WILSON, R., DINI, D. & VAN WACHEM, B. 2016 A numerical study exploring the effect of particle properties on the fluidization of adhesive particles. *AIChE J.* **62** (5), 1467–1477.

WINITZKI, S. 2003 Uniform approximations for transcendental functions. In *Computational Science and Its Applications – ICCSA 2003: International Conference Montreal, Canada, May 18–21, 2003 Proceedings, Part I* (ed. V. Kumar, M. L. Gavrilova, C. J. Kenneth Tan & P. L'Ecuyer), pp. 780–789. Springer.

YANG, L. L., PADDING, J. T. J. & KUIPERS, J. A. M. H. 2016 Modification of kinetic theory of granular flow for frictional spheres. Part I: two-fluid model derivation and numerical implementation. *Chem. Engng Sci.* **152**, 767–782.

YANG, R., ZOU, R. & YU, A. 2000 Computer simulation of the packing of fine particles. *Phys. Rev.* E **62** (3 Pt B), 3900–3908.

YE, M., VAN DER HOEF, M. A. & KUIPERS, J. A. M. 2005 From discrete particle model to a continuous model of geldart a particles. *Chem. Engng Res. Des.* **83** (7), 833–843.

ZHOU, Z. Y., KUANG, S. B., CHU, K. W. & YU, A. B. 2010 Discrete particle simulation of particle-fluid flow: model formulations and their applicability. *J. Fluid Mech.* **661**, 482–510.